INVESTIGATION OF RADIATIVE TRANSFER EFFECTS IN PHOTOIONIZED NEBULAE

by

ANDRI PROZESKY

submitted in accordance with the requirements
for the degree of

DOCTOR OF PHILOSOPHY

in the subject of

ASTRONOMY

at the

UNIVERSITY OF SOUTH AFRICA

Supervisor: PROF D P SMITS

2019

Declaration of originality

I declare that INVESTIGATION OF RADIATIVE TRANSFER EFFECTS IN PHOTOIONIZED NEBULAE is my own work and that all the sources that I have used or quoted have been indicated and acknowledged by means of complete references.

I further declare that I submitted the thesis to originality checking software and that it falls within the accepted requirements for originality.

I further declare that I have not previously submitted this work, or part of it, for examination at Unisa for another qualification or at any other higher education institution.

A. Prozesky

Summary

Detailed knowledge of the hydrogen population structure is necessary for the interpretation of hydrogen recombination line (HRL) observations. Calculations of hydrogen departure coefficients using a capture-collision-cascade type model with the angular momentum quantum levels resolved that includes the effects of external radiation fields are presented. The stimulating processes are important at radio frequencies and can influence level populations. Updated atomic rates and new numerical techniques with a solid mathematical basis have been incorporated into the model to ensure convergence of the solution. My results differ from previous results by up to 20 per cent. The effects on departure coefficients of continuum radiation from dust, the cosmic microwave background, the stellar ionising radiation, and free-free radiation are quantified.

Atomic hydrogen masers occur in recombination plasmas in sufficiently dense HII regions. These HRL masers have been observed in a handful of objects to date and the analysis of the atomic physics involved has been rudimentary. A new model of HRL masers is presented which uses an nl-model to describe the atomic populations interacting with free-free radiation from the plasma, and an escape probability framework to deal with radiative transfer effects. The importance of including the collisions between angular momentum quantum states and the free-free emission in models of HRL masers is demonstrated. The model is used to describe the general behaviour of radiative transfer of HRLs and to investigate the conditions under which HRL masers form. The model results show good agreement with observations collected over a broad range of frequencies. Theoretical predictions are made regarding the ratio of recombination lines from the same upper quantum level for these objects.

KEY WORDS: atomic data — atomic processes — line: formation — radiative transfer — radio lines: ISM — masers — methods: numerical — nebulae — ISM: atoms — HII regions

Contents

Chapter 1

Introduction

1.1 Hydrogen recombination lines

The understanding of the physics of ionised gasses is crucial to many subjects in astronomy. Emission spectra can be observed from numerous astronomical objects, and the interpretation of these spectra is essential to understand, and scientifically describe, them. The study of lines in these spectra has yielded valuable information regarding the most elementary atomic processes occurring in the Universe and has proven to be an essential tool in astronomy.

Photoionised nebulae are permeated by an external radiation field, generally from a nearby star or stars. The particles (atoms, ions and electrons) in the nebula and the photons of the radiation field interact in such way that the physical properties of the nebula can be deduced by studying the resultant light coming from the plasma. To model the theoretical spectrum that we would expect to see from a specific nebula, it is necessary to have detailed knowledge of the microscopic processes occurring within the nebula. These can be used to derive the relative number of electrons in each bound state of the atoms, called the level populations, which in turn give us the expected spectral line intensities under specific conditions.

A specific class of spectral lines arise when free electrons are captured by ions into energy levels with large principal quantum numbers. The electrons tend to

cascade to lower energy levels through radiative decay, emitting photons as they make downward transitions. Emission lines that result from this process in hydrogen atoms are called hydrogen recombination lines (HRLs). These lines are observed from photoionised gasses, where there are a large relative number of free electrons that can easily recombine to ions. HRLs are observed over a wide range of frequencies, from ultraviolet to radio. HRLs in the optical regime have been studied extensively, but the study of lower frequency lines is an emerging field in astronomy.

The construction of new radio telescopes such as MeerKAT, the Atacama Large Millimeter/submillimeter Array (ALMA) and the Low Frequency Array (LOFAR) provide new opportunities to study emission lines with improved sensitivity at low frequencies. Fig. 1.1 shows the H$n\alpha$ transitions (hydrogen transitions between principal quantum numbers $n+1 \rightarrow n$) that will be observable with each of these telescopes. Very low frequency ($\leq 1.4\,\mathrm{GHz}$) detections of hydrogen recombination lines are rare (Anantharamaiah, 2002), but carbon lines are commonly detected at these frequencies. Transitions in carbon produce lines with different frequencies to hydrogen, but reliable calculations of lines with $n \gtrsim 300$ are needed to interpret results from instruments such as LOFAR. An accurate model for low frequency HRLs is essential so that we are able to interpret observations and reap the full benefits of these high-quality measurements.

Atomic processes stimulated by photons become important for levels where low frequency lines form in hydrogen (Goldberg, 1966), yet these are often neglected in theoretical models. In extreme conditions, stimulated emission can become so efficient that maser action is observed in HRLs. The number of HRL masers that have been observed so far is small and the theoretical work that has been done on this is limited.

1.2 Motivation

Emission lines from photoionised nebulae contain a wealth of information on the conditions in the plasma, but to interpret observed spectra theoretical models of

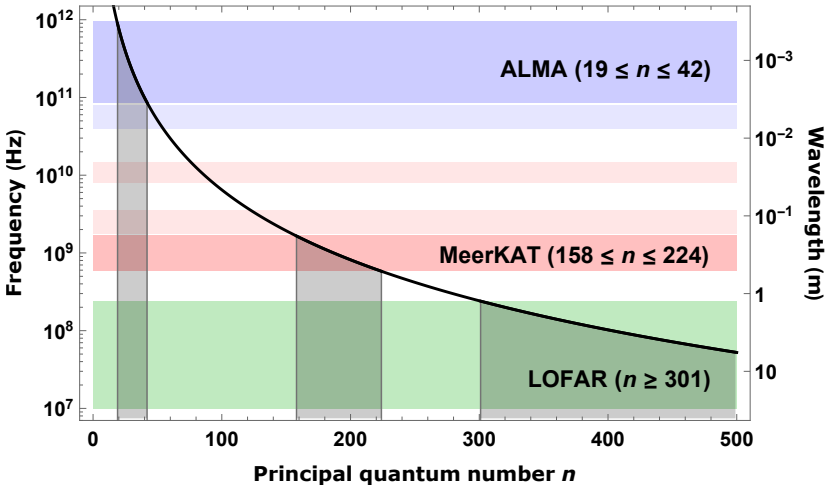

Figure 1.1 – The black line shows the frequencies (wavelengths) of H$n\alpha$ transitions as a function of n for hydrogen. The horizontal shaded bands depict the operating frequency bands of ALMA (blue), MeerKAT (red) and LOFAR (green). The lighter shaded bands are planned additions to the telescopes, but are not operational yet. The vertical grey shaded areas indicate the ranges of principal quantum number for which the H$n\alpha$ transitions will technically fall into the observing frequencies of the respective telescopes.

line intensities are required. HRLs are of great value to a wide variety of topics in astronomy. To be able to utilize this powerful tool to the fullest, a solid theoretical foundation is needed to interpret observations. The spectral line intensities that are observed depend on the level populations of the quantum states of the atoms or ions in the nebula. Accurate and robust models for the spectral line intensities, and thus the level populations, for the varied conditions under which they form are absolutely essential.

Goldberg (1966) showed that at low frequencies, where stimulated processes are important, the accuracy of the calculation of atomic level populations has a substantial influence on the theoretical intensities of recombination lines. This sentiment is echoed 50 years later by Sánchez Contreras et al. (2017) who also point out that there is disagreement between the results of various authors without one set of values clearly being the correct one.

The current models, such as that of Storey & Hummer (1995), work well for lines that are observed in the optical range, but need to be extended to be accurate for low frequency lines as well. A more sophisticated model should include all the important atomic processes that affect the level populations of an atom, specifically the effects of the stimulated processes. Presently, the only models that account for stimulated processes also neglect elastic collisions between angular momentum states of atoms. This assumption is valid for the very highest n-levels, but not appropriate for intermediate levels. More accurate updated atomic rates are available now that were not when previous models were constructed.

The most obvious application of HRL observations is to deduce the physical properties of the interstellar medium (ISM). The ISM has a very close relationship to stellar formation and death, and to know the conditions of the ISM accurately adds to the understanding of these important processes. About 90 % (by number) of the ISM is made up of hydrogen, with 10 % helium and less than 1 % of metals[1]. Low frequency recombination lines can be observed from various metals; in particular, observations of carbon have proved to be invaluable in the study of the cold ISM.

[1]The astronomical convention where all elements with atomic number greater than two are referred to collectively as "metals" is followed throughout this work.

The hydrogen atom can be modeled analytically and such a model is often used as a foundation for more complex models. For these reasons, this work will focus on the modelling of the hydrogen atom.

Most HRL studies are done on gaseous nebulae, which are mostly optically thin to line radiation. If HRLs form under conditions that are not optically thin, it is possible that the line photons interact significantly with atoms in the gas in such a way that HRL masers are observed. Hydrogen recombination masers are a relatively new field of study with only a handful of examples detected so far. There are some important differences between molecular and atomic masers, both on the macroscopic scale such as in the environments where they form, and at the atomic level such as the pumping mechanism and interaction of many masing lines. The theoretical framework for these objects is still developing and the aim of this work is to contribute to our understanding by constructing a theoretical model that specifically focuses on the atomic process rather than the geometry and kinematics.

1.3 Methodology

I created two computer programmes in the language C to simulate atomic physics present in photoionised nebulae under different physical conditions. The first is a capture-collision-cascade (C^3) type model. These are used to model homogeneous recombination nebulae. The model takes various atomic processes into account to calculate the level populations of hydrogen under specified physical conditions. The level populations can be used to calculate directly the theoretical spectral line intensities emitted by the plasma. My model includes the angular momentum structure of the atoms and the processes that occur between the l-states. This is known as an nl-model, as opposed to an n-model that assumes a statistical distribution in the l-states and is much simpler than an nl-model.

In the process of constructing the model, I derived a numerical method to verify that convergence has been reached when using an iterative method of solution for

a linear system of equations. Improved algorithms are developed and presented. The updated model results can differ quite significantly ($\sim 20\,\%$) with previously published results under certain conditions. I use updated atomic rates and, in particular, include the effects of stimulated processes. The model is used to investigate the effects of continuum fields that are commonly found in gaseous nebulae on the level populations. This model and the results derived from it are published in Prozesky & Smits (2018).

The second programme is an extension of the first and models HRL masers. The main difference between it and the first model is that it incorporates radiative transfer. This was done by using an escape probability approximation (EPA), an approach that has been applied extensively to model molecular masers. The model is used to examine the general trends and behaviour of HRL masers from an atomic physics perspective. The conditions where HRL masers can form are reviewed and observational diagnostics are presented that might aid in finding more observational examples. The main results from the maser model are published in Prozesky & Smits (2020).

1.4 Overview of thesis

Chapter 2 gives an overview of the theory that is used throughout this work. The various atomic processes that are included in the models are described and the details of how their rates are calculated are given. Radiative transfer theory as it relates to astronomical gasses is also discussed. The C^3 model is described in Chapter 3. This chapter outlines the work that has been done previously on level population calculations and includes new numerical techniques that have been incorporated into the model. In Chapter 4 the C^3 model results are compared to results published previously and the stimulating effects of continuum radiation fields within a nebula are examined.

A review of the work done so far on HRL masers is given in Chapter 5, as well as a description of the model that was used to simulate the atomic processes involved in

HRL maser formation. The main results of my maser model, as well as comparison with observations and predictions are given in Chapter 6. The main conclusions, as well as future projects based on this work, are outlined in Chapter 7.

Chapter 2

Atomic physics in photoionised nebulae

The spectra that are emitted from photoionised nebulae are dependent on the physical interactions that occur within the gas on an atomic scale. This chapter discusses the theoretical aspects of the various atomic processes that occur in the hydrogen atom, as well as the calculational details of each. An overview of the quantum mechanics of atomic transitions is given in section 2.1. Section 2.2 discusses the processes that involve the interaction between atoms and photons, called radiative processes, whereas the collisional processes between particles in the gas will be considered in section 2.3. The theory of radiative transfer in homogeneous gasses is reviewed in section 2.4. The quantum mechanical aspects are discussed in more detail in standard atomic physics textbooks, such as Bransden & Joachain (2003). The application of the physics to astronomical environments as well as the radiative transfer theory of low frequency spectral lines can be found in Gordon & Sorochenko (2009).

2.1 Quantum mechanics of atomic transitions

To be able to calculate the rates of transitions between two quantum mechanical states, the wave functions of both states need to be known. The time-independent

(non-relativistic) Schrödinger equation for a one-electron atom in a Coulomb potential can be solved exactly. Because the potential is spherically symmetric, the eigenfunctions ψ_{nlm} can be separated into a radial $R_{nl}(r)$ and angular part $Y_{lm}(\theta, \phi)$ of the form

$$\psi_{nlm} = R_{nl}(r)\, Y_{lm}(\theta, \phi) \tag{2.1}$$

where n, l and m are the principal, angular momentum and magnetic quantum numbers, respectively. The eigenvalues for the energy are given by

$$E_{nl} = -\frac{e^2}{2a_0 n^2}$$

for hydrogen, where e is the elementary charge and a_0 is the Bohr radius. The energy is degenerate with respect to l for a Coulomb field.

By Fermi's golden rule, and assuming the electric dipole approximation, the probability of an electron making a transition from an eigenstate $|\psi_\mathrm{i}\rangle$ to another state $|\psi_\mathrm{f}\rangle$ depends on the quantity

$$\langle\psi_\mathrm{f}|\,\mathbf{r}\,|\psi_\mathrm{i}\rangle = \int R_\mathrm{f} r R_\mathrm{i}\,\mathrm{d}r \int Y_\mathrm{f} Y_\mathrm{i}\,\mathrm{d}\Omega \tag{2.2}$$

where $\mathrm{d}\Omega = \sin\theta\,\mathrm{d}\theta\,\mathrm{d}\phi$ and the integrals are over all space. The angular integral can be evaluated explicitly and restricts the change of the angular momentum quantum number for the transition so that for an electric dipole transition $\Delta l = \pm 1$.

The transition probabilities of the various atomic processes depend on the quantity

$$\tau_\mathrm{i}^\mathrm{f} = \int_0^\infty R_\mathrm{f}\, r\, R_\mathrm{i}\,\mathrm{d}r,$$

which is called the radial dipole matrix element.

Atomic processes affecting the level populations can be grouped into two categories: bound-bound and bound-free. Bound-bound transitions occur between two bound electron states, so that E_i, $E_\mathrm{f} < 0$. In a bound-free transition, an electron is either captured by the atom from the continuum ($E_\mathrm{i} > 0$, $E_\mathrm{f} < 0$) or is ionised from a

bound state of the atom and becomes a free electron ($E_\mathrm{i} < 0$, $E_\mathrm{f} > 0$).

2.1.1 The bound-bound radial matrix element

The dipole radial matrix element for an electron transition between two bound states nl and $n'l'$, with $n > n'$ is defined by

$$\tau_{nl}^{n'l'} = \tau_{n'l'}^{nl} = \int_0^\infty R_{n'l'}\, r\, R_{nl}\, \mathrm{d}r$$

where R_{nl} is the normalized radial wave function for the electron state nl.

An explicit formula for the bound-bound matrix element of a transition between nl and $n'\, l-1$ for hydrogen is given by Gordon (1929) as

$$\begin{aligned}\tau_{nl}^{n'\,l-1} \;=\; & \frac{2^{2l}}{(2l-1)!}\left[\frac{\Gamma(n+l+1)\Gamma(n'+l)}{\Gamma(n-1)\Gamma(n'-l+l)}\right]^{1/2}(nn')^{l+1}\,(n+n')^{-n-n'}\,(n-n')^{n-l-2} \\ & \times (n'-n)^{n'-l}\left\{{}_2F_1\left[l+1-n,\, l-n',\, 2l,\, \frac{-4nn'}{(n-n')^2}\right]\right. \\ & \left. -\,{}_2F_1\left[l-1-n,\, l-n',\, 2l,\, \frac{-4nn'}{(n-n')^2}\right]\right\} \qquad (2.3)\end{aligned}$$

where ${}_2F_1$ is the Gaussian hypergeometric function. The matrix element $\tau_{nl}^{n'\,l+1}$ for a transition from $nl \rightarrow n'\,l+1$ is obtained by making the substitutions $n \rightarrow n'$ and $l \rightarrow l+1$ in the above formula, because $\tau_{nl}^{n'l'}$ is symmetric with respect to nl and $n'l'$.

Due to overflow errors in the calculation of the hypergeometric functions, direct calculation of the matrix elements $\tau_{nl}^{n'l'}$ using equation (2.3) is impractical for large principal quantum numbers. To avoid this an efficient iterative calculational scheme described by van Regemorter et al. (1979) is used.

The results were compared to the tables of Green et al. (1957) and agreed almost exactly. Wiese & Fuhr (2009) published relativistic transition probabilities and noted that their results are almost identical to those of Green et al. (1957).

2.1.2 The bound-free radial matrix element

The radial dipole matrix elements for transitions between a bound and a free state was obtained by Karzas & Latter (1961) by analytic continuation of equation (2.3) by letting $n' \rightarrow i\eta$. They introduced the parameter κ where $\kappa = 1/\eta$ so that the energy difference between the bound and free states is given by

$$\begin{aligned} E_{\rm f} - E_{\rm i} &= \left(\frac{1}{n^2} - \frac{1}{(i\eta)^2}\right)\chi_0 \\ &= \left(1 + n^2\kappa^2\right)\chi_{nl} \end{aligned} \tag{2.4}$$

where $\chi_{nl} = \chi_0/n^2$ is the ionisation energy of level nl and χ_0 is the ionisation energy of the ground state.

Burgess (1965) gives an explicit expression for $\tau_{nl}^{\kappa l \pm 1}$ as

$$\begin{aligned} \tau_{nl}^{\kappa l \pm 1} &= \frac{\exp\left[-\left(2/\kappa\right)\arctan\left(n\kappa\right)\right]}{4n^2\left(2l \pm 1\right)!}\left(\frac{4n}{1+n^2\kappa^2}\right)^{\min(l,l')+1} \\ &\times \left[\frac{\pi}{2}\frac{(n+l)!}{(n-l-1)!\left[1-\exp\left(-2\pi/\kappa\right)\right]}\prod_{s=0}^{l'}\left(1+s^2\kappa^2\right)\right]^{1/2} Y_{\pm} \end{aligned} \tag{2.5}$$

where

$$\begin{aligned} Y_+ &= i\eta\left(\frac{n-i\eta}{n+i\eta}\right)^{n-l}\left[{}_2F_1\left(l+1-n,\, l-i\eta,\, 2l+2,\, \frac{-4ni\eta}{(n-i\eta)^2}\right)\right. \\ &\left. - \left(\frac{n+i\eta}{n-i\eta}\right)^2 {}_2F_1\left(l+1-n,\, l+1-i\eta,\, 2l+2,\, \frac{-4ni\eta}{(n-i\eta)^2}\right)\right] \end{aligned}$$

and

$$\begin{aligned} Y_- &= \left(\frac{n-i\eta}{n+i\eta}\right)^{n-l-1}\left[{}_2F_1\left(l-1-n,\, l-i\eta,\, 2l,\, \frac{-4ni\eta}{(n-i\eta)^2}\right)\right. \\ &\left. - \left(\frac{n+i\eta}{n-i\eta}\right)^2 {}_2F_1\left(l+1-n,\, l-i\eta,\, 2l,\, \frac{-4ni\eta}{(n-i\eta)^2}\right)\right] . \end{aligned}$$

The hypergeometric series all have a finite number of terms, so the electric dipole

moment matrix elements for bound-free transitions, in principle, can be computed directly from equation (2.5). However, a large number of terms can occur, especially for large n and small l, making direct computation cumbersome.

Burgess (1965) presented a method that is based on recurrence relations that satisfies the exact matrix elements for hydrogenic atoms or ions. This method is more suitable for computational implementation than using equation (2.5) directly, and was used in this work.

Burgess (1965) observes that severe scaling problems can occur with this method for large n. This was overcome by doing calculations with the natural logarithm of the recurrence relations. The natural logarithm reduces the size of the numbers stored in the computer memory at intermediate steps and therefore prevents overflow errors. My results agreed with the tables given by Burgess (1965).

2.2 Radiative processes

2.2.1 Bound-bound transitions

Spontaneous emission

Bound electrons in excited energy levels can decay spontaneously to lower energy levels. To conserve the energy of the system, a photon is radiated away in an arbitrary direction with energy $h\nu$, equal to the energy difference between the two bound levels. Consider a spontaneous emission transition from an upper energy level nl to a lower level $n'l'$. The reaction can be represented by

$$X_{nl} \rightarrow X_{n'l'} + h\nu \,.$$

The rate of a spontaneous dipole transition from level nl to a lower energy level $n'l'$ is calculated using (Brocklehurst, 1971)

$$A_{nl,n'l'} = \frac{64\pi^4\nu^3}{3hc^3}\frac{\max(l,\, l')}{2l+1}e^2a_0^2\left[\tau_{nl}^{n'l'}\right]^2 \tag{2.6}$$

in cgs units, where h is Planck's constant, c is the speed of light in a vacuum and ν is the frequency of the emitted photon equal to

$$\nu = \frac{E_\mathrm{f} - E_\mathrm{i}}{h} \tag{2.7}$$

$$= cR_\mathrm{H}\left(\frac{1}{n'^2} - \frac{1}{n^2}\right) . \tag{2.8}$$

The Rydberg constant for a hydrogenic atom R_H is given by the Rydberg constant for a nucleus with infinite mass R_∞, scaled by the reduced mass of the nucleus μ with a total mass M, i.e.

$$R_\mathrm{H} = \frac{\mu}{m_\mathrm{e}} R_\infty \quad \text{where} \quad \mu = \frac{m_\mathrm{e} M}{m_\mathrm{e} + M} ,$$

where m_e is the mass of an electron.

The Einstein A-values for two n-levels, $A_{nn'}$, are obtained from equation (2.6) using

$$A_{nn'} = \frac{1}{n^2} \sum_{l=0}^{n-1} \sum_{l'=l\pm1} (2l+1)\, A_{nl,n'l'} . \tag{2.9}$$

For levels with $n > 500$, the approximations due to Menzel (1937) for the A-value and Gaunt factor are used, which are given by

$$A_{nn'} = \frac{16\alpha^4 c}{3\pi\sqrt{3}a_0} \frac{g_{nn'}}{n^3 n'(n^2 - n'^2)} \tag{2.10}$$

where α is the fine structure constant and $g_{nn'}$ is the bound-bound Gaunt factor that is approximated by

$$g_{nn'} = 1 - \frac{0.1728\,(1 + n'^2/n^2)}{(1 - n'^2/n^2)^{2/3}\,(n')^{2/3}} . \tag{2.11}$$

Because collisional processes will always dominate over radiative processes at these levels (for the conditions considered here), inaccuracies introduced by this approximation are not important.

Absorption

An electron initially in level $n'l'$ can make an upward transition to a higher level nl by absorbing a photon from an ambient radiation field,

$$X_{n'l'} + h\nu \rightarrow X_{nl}\,.$$

Einstein (1916) derived general relations between the rates of the bound-bound radiative processes. He showed that the probability of absorption is proportional to a factor $B_{n'l',nl}$ which can be written in terms of the probability of a spontaneous emission as

$$B_{n'l',nl} = \frac{g_{nl}}{g_{n'l'}}\frac{c^2}{2h\nu^3}A_{nl,n'l'} = \frac{2l+1}{2l'+1}\frac{c^2}{2h\nu^3}A_{nl,n'l'} \tag{2.12}$$

where

$$g_{nl} = \frac{2l+1}{n^2}$$

is the degeneracy of level nl[1].

Stimulated emission

In the presence of a radiation field an electron can be stimulated to make a downward transition, emitting a photon with the same frequency as the stimulating photon,

$$X_{nl} + h\nu \rightarrow X_{n'l'} + h\nu + h\nu\,.$$

Stimulated emission is the inverse process to absorption and is often included as a negative absorption.

Einstein (1916) showed that the stimulated emission coefficient $B_{nl,n'l'}$ is related to the absorption coefficient $B_{n'l',nl}$ and the spontaneous emission coefficient $A_{nl,n'l'}$

[1]The Einstein B-factors for absorption and stimulated emission was originally defined by Einstein in terms of energy density. In line with most astronomical texts, the definitions given here and used throughout this work are in terms of specific intensity I_ν.

by

$$B_{nl,n'l'} = \frac{g_{n'l'}}{g_{nl}} B_{n'l',nl} = \frac{c^2}{2h\nu^3} A_{nl,n'l'} \,. \tag{2.13}$$

2.2.2 Bound-free transitions

Radiative recombination

Radiative recombination is the process whereby an ion captures a free electron into a bound state with the excess energy being radiated away as a photon. If the electron is captured into an excited state of the atom, it will decay to the ground state by a number of radiative transitions. Let $X^{+(i)}$ be an i-times ionised atom. In the case of hydrogen, $X^{+(i)}$ is just the bare nucleus, a proton. Let $X_{nl}^{+(i-1)}$ represent an ion with a valence electron in the state nl. Radiative recombination is given by

$$X^{+(i)} + e^- \rightarrow X_{nl}^{+(i-1)} + h\nu \,.$$

The energy of the system has to be conserved, so the kinetic energy of the free electron and the energy of the emitted photon are related by

$$h\nu = \chi_{nl} + \tfrac{1}{2} m_\mathrm{e} v^2 \tag{2.14}$$

where χ_{nl} is the ionisation potential of the level nl of the atom and v is the free electron speed. The probability of a radiative recombination increases as the relative velocity between the free electron and ion decreases.

The radiative recombination rate to a level nl per unit volume is dependent on the cross-section for radiative recombination, $\sigma_{nl}^\mathrm{r}(v)$, for an electron with a velocity v. The total recombination rate coefficient α_{nl}^r is found by averaging the cross-section over the velocity distribution function $f(v)$ of the free electrons. The recombination rate also depends on the number densities of the free electrons and the protons, N_e and N_p respectively, and is given by

$$N_\mathrm{e} N_\mathrm{p} \alpha_{nl}^\mathrm{r} = N_\mathrm{e} N_\mathrm{p} \int \sigma_{nl}^\mathrm{r}(v) v f(v) \mathrm{d}v. \tag{2.15}$$

Bohm & Aller (1947) argued that in gaseous nebulae, collisions amongst the free electrons set up a Maxwellian distribution for these particles on time scales that are much shorter than other atomic processes. More recently, Nicholls et al. (2012) suggested that the long-standing discrepancy between electron densities and chemical abundances in planetary nebulae and HII regions, obtained from different techniques, can be resolved if a κ-distribution function is used for the free electrons instead of a Maxwellian. There is strong empirical evidence that κ-distributions are present in solar plasmas. However, at this stage there is little theoretical or observational evidence in favour of κ-distributions in photoionised nebulae (Zhang et al., 2016; Ferland et al., 2016; Draine & Kreisch, 2018). Therefore, in this work all velocity distribution functions are taken to be the Maxwellian distribution given by

$$f(v)\,\mathrm{d}v = 4\pi v^2 \left(\frac{m_\mathrm{e}}{2\pi k_\mathrm{B} T_\mathrm{e}}\right)^{3/2} e^{-m_\mathrm{e} v^2/(2k_\mathrm{B}T_\mathrm{e})}\mathrm{d}v\,,$$

where k_B is the Boltzmann constant and T_e is the kinetic temperature of the free electrons.

An expression for α^r_{nl} that uses a Maxwellian distribution with a temperature T_e for the free electron velocities is given by Burgess (1965) as

$$\alpha^\mathrm{r}_{nl} = \left(\frac{2\pi^{1/2}\alpha^4 a_0^2 c}{3}\right)\frac{2y^{1/2}}{n^2}\sum_{l'=l\pm1} I(n,\,l,\,l',\,T_\mathrm{e}) \tag{2.16}$$

where

$$I(n,\,l,\,l',\,T_\mathrm{e}) = \max(l,\,l')\;y\int_0^\infty \left(1+n^2\kappa^2\right)^2 \Theta(n,\,l;\,\kappa,\,l')\,\mathrm{e}^{-y\kappa^2}\mathrm{d}\left(\kappa^2\right) \tag{2.17}$$

and

$$y = \frac{R_\mathrm{H} hc}{k_\mathrm{B} T_\mathrm{e}}, \qquad \Theta(n,\,l;\,\kappa,\,l') = \left(1+n^2\kappa^2\right)\left|\tau^{\kappa l'}_{nl}\right|^2 . \tag{2.18}$$

The integration in equation (2.17) is performed using a Gaussian integration technique. The integrands vary very rapidly when κ is small, and much slower for large κ. Following Burgess (1965), a number of five-point Gaussian integrations are made, starting with an interval size of $h = 10^{-4}n^{-1}$. The interval size is dou-

bled after every five-point integration and the procedure is terminated when the sum of the integrals is accurate to six significant digits.

The total radiative recombination coefficient into an energy level n is given by the sum of the partial coefficients over the angular momentum states so that

$$\alpha_n^{\mathrm{r}} = \sum_{l=0}^{n-1} \alpha_{nl}^{\mathrm{r}} \,. \tag{2.19}$$

Photoionisation

Photoionisation is analogous to the bound-bound process of absorption. This process involves a bound electron of an atom being liberated to the continuum from level nl due to the absorption of a photon,

$$X_{nl}^{+(i-1)} + h\nu \rightarrow X^{+(i)} + e^- \,.$$

The ionising photon has to have a higher energy, and thus higher frequency, than one involved in a bound-bound absorption reaction from the same level, as the incoming photon has to have sufficient energy to lift the electron to a free state, as described by equation (2.14).

The rate of photoionisations per unit volume out of bound level nl of a atom or ion will depend on the number density N_{nl} of atoms or ions in the state nl. For a plasma in an ambient radiation field with mean intensity J_ν, the number of photons in the frequency interval ν to $\nu + \mathrm{d}\nu$ that can ionise an atom is $4\pi J_\nu \mathrm{d}\nu/(h\nu)$. Only photons with energies higher than χ_{nl} will be able to ionise an electron from state nl. Let $a_{nl}^{\mathrm{p}}(\nu)$ be the photoionisation cross-section from level nl for a photon with frequency ν, then the rate of photoionisations per unit volume is given by

$$N_{nl}\alpha_{nl}^{\mathrm{p}} = N_{nl} \int_{\chi_{nl}/h}^{\infty} a_{nl}^{\mathrm{p}}(\nu) \frac{4\pi J_\nu}{h\nu} \mathrm{d}\nu \,. \tag{2.20}$$

The photoionisation cross-section to level nl for a hydrogenic atom is calculated

using the formula of Burgess (1965), which is given by

$$a_{nl}^{\mathrm{p}}\big(\kappa^2\big) = \left(\frac{4\pi\alpha a_0^2}{3}\right) n^2 \sum_{l'=l\pm1} \frac{\max(l,\, l')}{2l+1}\, \Theta(n,\, l;\, \kappa,\, l')\ . \tag{2.21}$$

Putting equation (2.21) into (2.20), and using equation (2.4), the photoionisation coefficient α_{nl}^{p} can be written as

$$\alpha_{nl}^{\mathrm{p}} = \left(\frac{4\pi R_{\mathrm{H}} c\alpha a_0^2}{3}\right) \frac{n^2}{2l+1} \int_0^\infty \left(\frac{4\pi J_\nu}{h\nu}\right)_{\kappa^2} \sum_{l'=l\pm1} \max(l,\, l')\, \Theta(n,\, l;\, \kappa,\, l')\, \mathrm{d}\big(\kappa^2\big)\ , \tag{2.22}$$

where the function $\Theta(n,\, l;\, \kappa,\, l')$ is given in equation (2.18). The subscript κ^2 indicates that the quantity inside the brackets should be written in terms of κ^2 before integration. The integral in equation (2.22) is handled in the same manner as for radiative recombination.

The total photoionisation coefficient for hydrogen from level n is given by

$$\alpha_n^{\mathrm{p}} = \sum_{l=0}^{n-1} \frac{2l+1}{n^2} \alpha_{nl}^{\mathrm{p}}\,. \tag{2.23}$$

Stimulated recombination

A free electron can be stimulated by a photon from the ambient radiation field to recombine to a bound level of an ion with a process analogous to stimulated emission

$$X^{+(i)} + e^- + h\nu \rightarrow X_{nl}^{+(i-1)} + h\nu + h\nu\,.$$

Let $\sigma_{nl}^{\mathrm{s}}(v)$ be the cross-section for stimulated recombination of an electron with a speed v into level nl. To obtain the total rate of stimulated recombination, the cross-section needs to be averaged over the free electron velocity distribution, as the chances of a stimulated recombination depends on the velocity of the recombining electron. For a radiation field with mean intensity J_ν the number of photons that can stimulate such a recombination is $4\pi J_\nu\, \mathrm{d}\nu/(h\nu)$. The speed of the free electron

and the frequency of the emitted photon are related by equation (2.14). This leads to $\mathrm{d}v = h/(mv)\,\mathrm{d}\nu$. Putting all of this together gives the rate at which stimulated recombinations occur as

$$N_\mathrm{e} N_\mathrm{p} \int_{\chi_{nl}/h}^{\infty} \frac{4\pi J_\nu}{h\nu} \sigma_{nl}^\mathrm{s}(v)\, f(v) \frac{h}{m} \mathrm{d}\nu = N_\mathrm{e} N_\mathrm{p} \alpha_{nl}^\mathrm{s}\,. \tag{2.24}$$

The cross-section for stimulated recombination $\sigma_{nl}^\mathrm{s}(v)$ of an electron with a speed v into level nl is related to the photoionisation cross-section a_{nl}^p (see equation (2.21)) by the Einstein-Milne relation (Milne, 1924)

$$\sigma_{nl}^\mathrm{s} = \frac{g_{nl}}{8\pi g_\mathrm{p}} \frac{h^2}{m_\mathrm{e}^2 v^2} a_{nl}^\mathrm{p}\,, \tag{2.25}$$

where g_p is the degeneracy of the proton.

Putting equation (2.21) into (2.25) gives the stimulated recombination cross-section, and in turn putting the result into equation (2.24) gives the stimulated recombination coefficient as

$$\begin{aligned}\alpha_{nl}^\mathrm{s} = {} & \left(\frac{4\pi R_\mathrm{H} c \alpha a_0^2}{3}\right) \left(\frac{m_\mathrm{e}}{2\pi k_\mathrm{B} T_\mathrm{e}}\right)^{3/2} \left(\frac{h}{m_\mathrm{e}}\right)^3 n^2 \\ & \times \int_0^\infty \left(\frac{4\pi J_\nu}{h\nu}\right)_{\kappa^2} \sum_{l'=l\pm1} \max(l,\, l')\, \Theta(n,\, l;\, \kappa,\, l')\, e^{-y\kappa^2} \mathrm{d}(\kappa^2)\end{aligned}$$

The integration is evaluated numerically using a Gaussian quadrature scheme as described above for radiative recombination.

The total stimulated recombination coefficient to an energy level n of hydrogen is given by

$$\alpha_n^\mathrm{s} = \sum_{l=0}^{n-1} \alpha_{nl}^\mathrm{s}\,. \tag{2.26}$$

2.3 Collisional transitions

2.3.1 Bound-bound transitions

Inelastic collisions

An unbound electron may interact with a bound electron, causing the bound electron to make a transition from one energy level to another. The free electron will either absorb or transfer energy to the bound electron in such a way that the kinetic energy of the free electron changes to conserve the energy of the system. The processes of collisional excitation and de-excitation are given by

$$X_{nl} + e^-_E \leftrightarrows X_{n'l'} + e^-_{E'} \,.$$

Let nl and $n'l'$ be two atomic levels with $n > n'$. The cross-section for such an excitation $\sigma_{n'l',nl}$ is a function of the free electron's velocity v, and is zero if the electron's energy is below $E_{n'l',nl} = h\nu_{n'l',nl}$. Electrons are more efficient than protons at inducing inelastic collisions in astrophysical nebulae (Osterbrock & Ferland, 2006).

The collisional excitation rate coefficient $C_{n'l',nl}$ is obtained by averaging the cross-section over the velocity distribution, that is

$$C_{n'l',nl} = \int \sigma_{n'l',nl}\,(v)\, v f(v)\, \mathrm{d}v \,.$$

The collisional excitation rate per unit volume depends on the number density of the free electrons and the atoms in the initial state $n'l'$ and is given by

$$N_\mathrm{e} N_{n'l'} C_{n'l',nl} \,.$$

For a system in local thermodynamic equilibrium (LTE) at temperature T_e, the

level populations will follow a Boltzmann distribution

$$\frac{N_{nl}}{N_{n'l'}} = \frac{g_{nl}}{g_{n'l'}} e^{-(E_{nl}-E_{n'l'})/k_{\rm B}T_{\rm e}} \,. \tag{2.27}$$

Let $C_{nl,\,n'l'}$ be the collisional de-excitation rate. The principle of detailed balance requires that

$$N_{nl}C_{nl,n'l'} = N_{n'l'}C_{n'l',nl}$$

in LTE. Substituting equation (2.27) for $N_{n'l'}/N_{nl}$ in the above equation yields a relationship between the coefficients for excitation and de-excitation which is given by

$$C_{nl,n'l'} = \frac{2l'+1}{2l+1} e^{-(E_{nl}-E_{n'l'})/k_{\rm B}T_{\rm e}} C_{n'l',nl} \,. \tag{2.28}$$

The semi-empirical formulae of Vriens & Smeets (1980) are used to calculate the rates for collisional de-excitation $C_{nn'}$ between the bound states n and n'. These values are valid over a wider range of temperatures than the values obtained from the formulae of Gee et al. (1976) which were used by Storey & Hummer (1995) (hereafter SH95). Vriens & Smeets (1980) claim that their results agree within 5 to 20 per cent with those of Gee et al. (1976) in the regimes where both calculations are valid.

SH95 resolved the collision rates between angular momentum states using

$$C_{nl,n'l'} = \frac{A_{nl,n'l'}}{A_{nn'}} C_{nn'} \tag{2.29}$$

for $\Delta l = \pm 1$. SH95 used this approximation for transitions with $n' = n \pm 1$ and

$$C_{nl,n'l'} = C_{nn'} \quad \text{for} \quad n' \neq n \pm 1 \,. \tag{2.30}$$

In my calculations the approximation in equation (2.29) is used throughout; detailed balance is used to calculate the rates of the inverse process. I included interactions between all levels with $n \neq n'$. Because elastic collision rates are higher than inelastic collision rates for all n for which collisions are important, l-levels are populated predominantly by angular momentum-changing collisions, and, hence,

the exact dependence of the inelastic collision rates on angular momentum is not that important.

Elastic collisions

Collisions between free particles and atoms occur, where angular momentum, but not energy, is transferred. Such a transition can be induced by any free particle that is able to carry away angular momentum. For a colliding particle labelled q, the reaction can be written as

$$X_{nl} + \mathrm{q}_E \rightarrow X_{nl'} + \mathrm{q}_E \,.$$

The rate per unit volume at which these transitions occur depends on the number density of the colliding particles and the atoms in the initial state nl and is given by

$$N_\mathrm{q} N_{nl} C_{nl,nl'} \,.$$

Protons are more efficient than electrons in distributing angular momentum (Pengelly & Seaton, 1964). Neutral particles interact much less strongly than charged particles through this process, so their effects are neglected.

The semi-classical impact-parameter formulation developed by Pengelly & Seaton (1964) for the rates of angular momentum changing collisions has been considered definitive for many decades. Recently, Vrinceanu et al. (2012) presented updated formulae for these transition rates for both the quantum and semi-classical case. Guzmán et al. (2016) did an in-depth analysis of the two approaches and concluded that the analytic equations presented in Pengelly & Seaton (1964) are much faster to compute and agree very well with the exact quantum mechanical probabilities of Vrinceanu et al. (2012). This agreed with an earlier conclusion of Storey & Sochi (2015a).

Brocklehurst (1971) used an iterative scheme to calculate the partial rate coefficients $C_{nl,nl\pm1}$ based on the work of Pengelly & Seaton (1964). Hummer &

Storey (1987) pointed out that this method caused oscillatory behaviour in the rate coefficients as a function of l. They avoided this by normalizing the collision cross-sections with the oscillator strengths of the transitions.

In this work, the formalism of Pengelly & Seaton (1964) is followed based on the recommendation of Storey & Sochi (2015b) and Guzmán et al. (2016). The modification suggested by Guzmán et al. (2016) to get the partial rates directly is utilized. The relevant equations in cgs units are

$$C_{nl,nl'} = 9.93 \times 10^{-6} \sqrt{\frac{\mu}{m_\mathrm{q}}} \frac{D_{nl,nl'}}{\sqrt{T_\mathrm{e}}} N_\mathrm{e} \times \left[11.54 + \log_{10} \left(\frac{m_\mathrm{q} T_\mathrm{e}}{\mu D_{nl,nl'}} \right) + 2 \log_{10} \left(R_\mathrm{c} \right) \right] \tag{2.31}$$

with

$$D_{nl,nl'} = \left(\frac{Z_\mathrm{q}}{Z_\mathrm{t}} \right)^2 \frac{6n^2 \max(l,\, l') \left[n^2 - \max(l,\, l')^2 \right]}{2l+1} \tag{2.32}$$

where m_q and Z_q are the mass and charge of the projectile particle, Z_t is the charge of the target atom or ion, μ is the reduced mass of the colliding system, and R_c is the effective cut-off radius of the interaction at large impact parameters as given by Pengelly & Seaton (1964).

In practice, $C_{nl,nl+1}$ is calculated using equation (2.31) and $C_{nl,nl-1}$ is obtained using the principle of detailed balance

$$C_{nl,\,nl'} = \frac{2l'+1}{2l+1} C_{nl',\,nl}\,. \tag{2.33}$$

Fig. 2.1 shows a comparison between the elastic collision rate coefficients as calculated using the method of Brocklehurst (1971) and the one used in this work for $n = 15$. The oscillatory behaviour of the former values can be seen clearly.

2.3.2 Bound-free transitions

If a colliding electron has sufficient energy when it interacts with a bound electron, it can liberate a bound electron to the continuum by a process called collisional

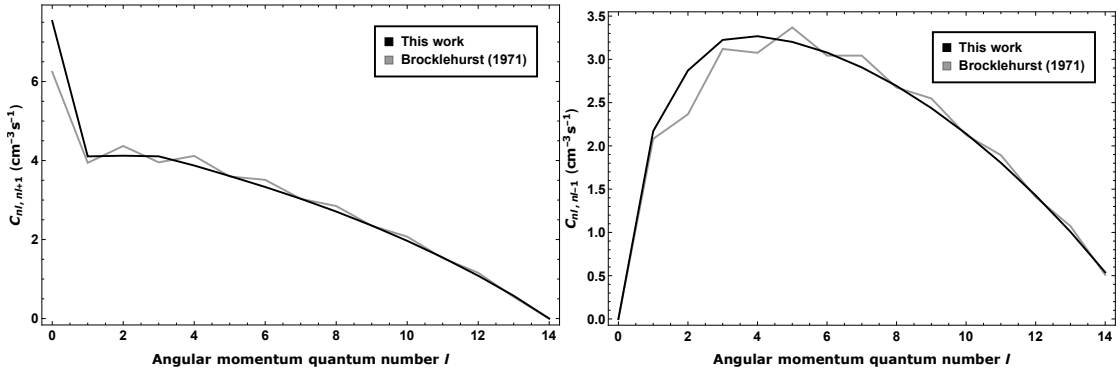

Figure 2.1 – Comparison between the elastic collision rate coefficients for $n = 15$ as used by Brocklehurst (1971) (grey) and in this work (black). The coefficients for transitions $nl \rightarrow nl+1$ are shown in the left panel and $nl \rightarrow nl-1$ in the left panel.

ionisation. Collisional ionisation is given by the forward reaction in

$$X^{+(i-1)} + e^-_E \leftrightarrows X^{+(i)} + e^-_{E'} + e^-_{E''} \,.$$

The backward reaction represents the inverse process of collisional ionisation, namely three-body recombination.

The collisional ionisation rate coefficient out of level nl, $C_{nl,i}$, is given by the collisional ionisation cross-section, $\sigma_{nl,i}$, for a bound level nl by a free electron with velocity v, averaged over the free electron distribution function so that

$$C_{nl,i} = \int \sigma_{nl,i}\,(v)\, v f(v)\, \mathrm{d}v \,.$$

The collisional excitation rate per unit volume depends on the number density of the free electrons and the atoms in the initial state nl and is given by

$$N_\mathrm{e} N_{nl} C_{nl,i} \,.$$

Because three-body recombination requires two free electrons and an ion, the rate is given by

$$N_\mathrm{e}^2 N_\mathrm{p} C_{i,nl} \,.$$

The Saha-Boltzmann equation for hydrogen relates the number density of atoms in level nl to the number density of the free electrons N_e and protons N_p present in a gas in LTE at temperature T_e

$$\frac{N_{nl}}{N_\mathrm{e}N_\mathrm{p}} = \frac{g_{nl}}{g_\mathrm{e}g_\mathrm{p}} \left(\frac{h^2}{2\pi m_\mathrm{e} k_\mathrm{B} T_\mathrm{e}} \right)^{3/2} e^{\chi_{nl}/k_\mathrm{B}T_\mathrm{e}} , \tag{2.34}$$

where χ_{nl} is the ionisation energy of level nl. The degeneracy of an electron is $g_\mathrm{e} = 2$ to account for the two possible spin states of an electron. The degeneracy of the proton g_p is taken as 1. The proton spin serves as a reference, with the spin of an electron being either parallel or anti-parallel to the proton spin.

In LTE the principle of detailed balance requires that

$$N_\mathrm{e}N_{nl}C_{nl,i} = N_\mathrm{e}^2 N_\mathrm{p} C_{i,nl} \, .$$

Using the Saha-Boltzmann equation (2.34) to relate N_e, N_i and N_{nl} for hydrogen, this gives

$$(2l+1)\, e^{\chi_{nl}/k_\mathrm{B}T_\mathrm{e}} C_{nl,i} = \left(\frac{2\pi m_\mathrm{e} k_\mathrm{B} T_\mathrm{e}}{h^2} \right)^{3/2} C_{i,nl} \, .$$

I use the rates of collisional ionisation $C_{n,i}$ from the formulae of Vriens & Smeets (1980). Because this process is never significant at the conditions considered here, the assumption $C_{nl,i} = C_{n,i}$ is used in the nl-model. The three-body recombination rates $C_{i,n}$ and $C_{i,nl}$ are obtained from detailed balance considerations. Vriens & Smeets (1980) found that their formulae for the bound-free collisional rates agreed with experimental data to within 10 to 30 per cent.

2.4 Radiative transfer

The theory of radiative transfer describes the transport of electromagnetic radiation through a medium. As radiation moves through a medium, it can interact with the particles of the medium through the various processes described above. If the radiation does not interact with the particles in the medium, the medium is

said to be optically thin, and the radiative transfer problem is greatly simplified. If there is a significant interaction the medium is optically thick. In an optically thick gas the intensity of radiation at any frequency will usually be decreased as a function of increasing distance. Under very specific circumstances, the intensity can be enhanced at specific frequencies. The latter instance will be considered in more detail in Chapter 5.

The equation of radiative transfer (ERT) describes the change in specific intensity along a given ray as it travels through a medium and is given by

$$\frac{\mathrm{d}I_\nu}{\mathrm{d}\tau_\nu} = S_\nu - I_\nu, \tag{2.35}$$

where I_ν is the specific intensity. For a homogeneous gas the specific intensity is equal to the mean specific intensity so that $I_\nu = J_\nu$. Because this work only deals with homogeneous media, J_ν will be used throughout. The source function is defined as

$$S_\nu = j_\nu/\kappa_\nu \,,$$

where the net (line + continuum) volume emission and absorption coefficients at the frequency ν are given by j_ν and κ_ν, respectively. The optical depth is defined as

$$\tau_\nu = \int_0^L \kappa_\nu \,\mathrm{d}l \,,$$

where the integral is along the path of the ray. For a homogeneous medium of thickness L the optical depth is given by

$$\tau_\nu = L\kappa_\nu \,. \tag{2.36}$$

A medium is considered optically thin if $\tau_\nu \ll 1$ and optically thick if $\tau_\nu \gg 1$.

The total line emission coefficient $j_{nn'}$ describes radiation added to the radiation of the spectral line of the transition $n \to n'$ through spontaneous emissions and is

defined as

$$j_{nn'} = \frac{h\nu}{4\pi} \sum_{l=0}^{n-1} \sum_{l'=l\pm1} b_{nl} N^*_{nl} A_{nl,n'l'} \tag{2.37}$$

N^*_{nl} is the population of level nl in LTE and b_{nl} is the departure coefficient of level nl which will be discussed in more detail in Section 3.2.

The total line absorption coefficient $\kappa_{n'n}$ gives the contribution of stimulated emissions ($B_{nn'}$) and absorptions ($B_{n'n}$) to the emerging radiation field as

$$\kappa_{n'n} = \frac{h\nu}{4\pi} \left(N_{n'} B_{n'n} - N_n B_{nn'}\right) \tag{2.38}$$

$$= \frac{h\nu}{4\pi} \sum_{l=0}^{n-1} \sum_{l'=l\pm1} b_{n'l'} N^*_{n'l'} B_{n'l',nl} \left(1 - \frac{b_{nl}}{b_{n'l'}} \mathrm{e}^{-h\nu/k_\mathrm{B}T_\mathrm{e}}\right) . \tag{2.39}$$

From the definition in equation (2.38), it is clear that $\kappa_{n'n}$ can become negative if the number of stimulated emissions exceeds the number of absorptions, thereby tending to increase the line intensity. The term inside brackets in equation (2.39) is the correction for stimulated emission.

Each transition has a well defined frequency $\nu_{nn'}$ associated with it, but in practice there is a range of frequencies around $\nu_{nn'}$ where photons from the line transition can be either emitted or absorbed. The emission and absorption coefficients at any particular frequency within the line are described by

$$j^\nu_{nn'} = j_{nn'} \phi_\nu \quad \text{and} \quad \kappa^\nu_{n'n} = \kappa_{n'n} \phi_\nu \, . \tag{2.40}$$

Strictly speaking, the normalised line profile functions ϕ_ν for emissions and absorptions are not equal, but they are similar enough for the purpose of this discussion that they will be considered to be equal.

At low enough frequencies, when the continuum emitted by the free electrons is significant, which usually occurs in the Rayleigh-Jeans limit, the line and continuum radiation are formed together. This means the net quantities (indicated by

subscript ν) in equation (2.35) must take into account the contributions of both the line radiation and the continuum (indicated by subscript c), so that

$$\kappa_\nu = \kappa^\nu_{n'n} + \kappa_\mathrm{c}, \qquad j_\nu = j^\nu_{nn'} + j_\mathrm{c}\,. \tag{2.41}$$

The net source function S_ν is given by

$$S_\nu = \frac{j^\nu_{nn'} + j_\mathrm{c}}{\kappa^\nu_{n'n} + \kappa_\mathrm{c}}\,. \tag{2.42}$$

For a homogeneous medium with no background radiation, the ERT equation (2.35) can be solved to give the total emission at any frequency

$$J_\nu = S_\nu \left(1 - e^{-\tau_\nu}\right)\,. \tag{2.43}$$

Equation (2.43) is not strictly valid close to the edge of a medium, where the radiation can no longer be considered to be isotropic. As a simplifying assumption, edge effects will not be considered in this work. For most applications, the interesting information contained in J_ν is the contribution of the line emission. It is usual to calculate the line intensity at a specific frequency by subtracting the continuum from the total intensity using

$$\bar{J}^\nu_{nn'} = S_\nu \left(1 - e^{-\tau_\nu}\right) - B_\nu \left(1 - e^{-\tau_\mathrm{c}}\right)\,, \tag{2.44}$$

where B_ν is the Planck distribution function, see for example Goldberg (1966) and Strelnitski et al. (1996a). However, if the gas becomes optically thick, the continuum photons interact with the atoms in a significant way so that the contribution of the line photons to the total intensity at line centre is

$$J^\nu_{nn'} = \left(\frac{j^\nu_{nn'}}{\kappa^\nu_{n'n} + \kappa_\mathrm{c}}\right)\left(1 - e^{-\tau_\nu}\right)\,. \tag{2.45}$$

Similarly, the contribution of the continuum photons will be

$$J^\nu_\mathrm{c} = \left(\frac{j_\mathrm{c}}{\kappa^\nu_{n'n} + \kappa_\mathrm{c}}\right)\left(1 - e^{-\tau_\nu}\right)\,. \tag{2.46}$$

Equations (2.45) and (2.46) account for the fact that the mean free path of a photon depends only on its frequency, not on its origin. The line intensity $J^{\nu}_{nn'}$ described by equation (2.45) cannot be measured directly from a spectrum. Therefore the quantity $\bar{J}^{\nu}_{nn'}$ described by equation (2.44) will be referred to as the observable line intensity under optically thick conditions.

From an observational perspective, only the quantity described by equation (2.44), which will be called the observable intensity, can be extracted from an observed spectrum. This is true even if the radiation is emitted from an optically thick region where maser effects are important. A comparison between the behaviour of $\bar{J}^{\nu}_{nn'}$ and $J^{\nu}_{nn'}$ is discussed in section 6.1.2.

In my models, the continuum absorption coefficient $\kappa_{\rm c}$ in the Rayleigh-Jeans regime is calculated using the expression of Oster (1961) given in cgs units by

$$\kappa_{\rm c} = \left(\frac{N_{\rm e}N_{\rm p}}{\nu^2}\right)\left(\frac{8e^6}{3\sqrt{3}m_{\rm e}^3c}\right)\left(\frac{\pi}{2}\right)^{1/2}\left(\frac{m_{\rm e}}{kT_{\rm e}}\right)^{3/2}\langle g\rangle \ . \tag{2.47}$$

For $T_{\rm e} < 550\,000\,{\rm K}$, the Gaunt factor averaged over a Maxwellian velocity distribution (Oster, 1961) can be approximated by

$$\langle g\rangle \approx \frac{\sqrt{3}}{\pi}\ln\left[\left(\frac{2kT_{\rm e}}{\gamma m_{\rm e}}\right)^{3/2}\frac{m_{\rm e}}{\pi\gamma e^2\nu}\right] \ , \tag{2.48}$$

where γ is the exponential of the Euler–Mascheroni constant. The continuum emission coefficient is given by

$$j_{\rm c} = \kappa_{\rm c}B_{\nu}(T_{\rm e}) \, .$$

Chapter 3

Capture-collision-cascade model

3.1 Development of level population calculations

The development of the calculations of the population structure of the hydrogen atom under nebular conditions has been heavily dependent on computational capabilities. Rosseland (1926) was the first to set up statistical equilibrium equations between energy levels for a gas not in LTE. The first C^3 model was constructed by Plaskett (1928) who considered levels up to $n = 7$. Plaskett (1928) estimated the recombination rate coefficients from observed intensities of spectral lines and accounted for spontaneous emission by all allowed routes. This is an n-model, meaning that it is implicitly assumed that the angular momentum levels are statistically populated according to

$$N_{nl} = N_n \frac{2l+1}{n^2} \,.$$

This is known as an n-model, as opposed to an nl-model where the transitions between the angular momentum states are considered explicitly.

The concept of using departure coefficients to denote the ratio of the population of a level to the populations which would be expected in LTE was introduced by Menzel (1937). A later paper in the same series (Baker & Menzel, 1938) gives the results for the departure coefficients calculated for a radiative model, i.e. where

levels are populated by radiative recombination and depopulated by spontaneous decay only. This is an n-model, and departure coefficients are given up to $n = 30$. The model approximates the contribution of energy levels up to the continuum. Their calculations contain a number of errors (Burgess, 1958).

Burgess (1958) performed calculations for an nl-model and resolved the angular momentum states for $n \leq 12$. He found that the populations of low levels deviated significantly from the statistical distributions expected in LTE. This is a radiative model, but it incorporates the two photon process for $2s \rightarrow 1s$ transitions and the collisional transition $2s \rightarrow 2p$ to counter the artificial overpopulation of the $2s$ level. Only transitions between states with $n \leq 12$ were considered in the calculation. Burgess (1958) points out that collisional processes become more important as n increases and that the departure coefficients tend to unity for large values of n.

Seaton (1959) improved the accuracy of the radiative n-model calculations of Baker & Menzel (1938) by introducing a cascade matrix technique for dealing with the capture-cascade equations. This allowed him to easily account for transitions via all possible routes of downward cascade. He took an infinite number of levels into account and extended the calculations to lower temperatures.

This work was later extended (Seaton, 1964) to a C^3 model and included the effects of collisions between the hydrogen atoms and free particles using a differential method. Additionally to radiative capture and cascade, the calculations of Seaton (1964) also account for collisional processes between adjacent energy levels ($n \rightarrow n \pm 1$), collisions between angular momentum states ($nl \rightarrow nl \pm 1$) as well as collisional ionisation and three-body recombination. Seaton (1964) and others (Dyson, 1967; Hoang-Binh, 1968) used a method where the rate equations were approximated with a second order differential equation. Sejnowski & Hjellming (1969) show that approximations made to render the differential equation tractable give rise to significant errors in the results.

In the radio regime Reber & Greenstein (1947); Wild (1952); van de Hulst (1945) indicated that spectral lines would be undetectable due to the effects of Stark broadening, and that the line-to-continuum intensity of these lines would either be too low to detect, or that the lines would merge together. Kardashev (1959)

calculated line widths and intensities using a different approach to Stark broadening and concluded that they would indeed be observable. Subsequently, HRLs in the radio regime were detected (Sorochenko & Borodzich, 1965; Dravskikh et al., 1965; Hoglund & Mezger, 1965; Lilley et al., 1966) and the focus of departure coefficient calculations shifted towards extending the results, which had focused on the optical regime, to higher principal quantum numbers relevant to radio lines.

Hoang-Binh (1968) found that inelastic collisional transitions with $\Delta n = |n - n'| > 1$ appreciably influence the populations of high energy levels and performed calculations not only from adjacent levels but from levels with $\Delta n = 1$, 2, 3. Sejnowski & Hjellming (1969) introduced an iterative method for calculating the departure coefficients up to $n = 260$ and considered collisional transitions up to $\Delta n = 20$ explicitly.

Brocklehurst (1970) made authoritative n-model calculations by allowing for radiative and collisional transitions from and to all levels by considering the rate equations in matrix form. He used a matrix condensation technique developed by Burgess & Summers (1969) to make it possible to account for a large number of energy levels with the computing power available at the time. Brocklehurst (1971) extended his calculations to an nl-model for levels with $n \leq 40$ by including collisional redistribution of angular momentum which used the results of the n-model as initial values for an iterative process for the nl-model.

An important step was taken by Burgess & Summers (1976) who included stimulated emission and absorption terms for the bound-bound and bound-free transitions in an n-model that went up to principal quantum number $n = 500$. They found that stimulated processes can have a significant effect on the values of the departure coefficients. This work was expanded by Summers (1977) who resolved the angular momentum states for levels with $n \leq 35$, but only considered how the ^{1}S, ^{2}S and ^{2}P levels of hydrogen were affected by a stellar radiation field.

Brocklehurst & Salem (1977a) and Salem & Brocklehurst (1979) published their programme and tables based on the n-model of Brocklehurst (1970) that gave departure coefficients for $50 \leq n \leq 300$. The programme included updated collisional cross sections from Gee et al. (1976), elastic collisions due to protons, as

well as radiative processes involving an external field, but did not consider angular momentum changing collisions. The programme was modified by Walmsley (1990) to generate results down to $n = 20$ and for higher densities than previously considered.

Storey & Hummer (1995) (hereafter SH95) performed accurate calculations and published extensive tables of departure coefficients for a variety of physical conditions. Their calculations follow a similar approach to Brocklehurst (1971). The results of SH95 are considered to be the definitive values for optical/IR recombination lines, but stimulated processes are not included in their model. However, the values of SH95 are being used to study low frequency lines (Fujiyoshi et al., 2006; Bendo et al., 2017; Sánchez Contreras et al., 2017, see for example). In Chapter 4 I present results using a model that includes stimulated and absorption processes in the bound-bound and bound-free transitions in an nl-model, and use updated numerical methods. The current calculated values differ significantly from those of SH95 for levels with principal quantum number $n \gtrsim 30$.

3.2 Departure coefficients

To determine theoretical line intensities, the level populations N_{nl} of all bound states need to be calculated. The level populations N_{nl} are calculated assuming statistical equilibrium which requires that the total rate of all transitions into any particular level must equal the total rate of transitions out of that level.

Menzel (1937) introduced a correction factor, denoted by b_{nl}, to compensate for the degree of departure from LTE of the level population from the LTE value N^*_{nl} so that

$$b_{nl} = \frac{N_{nl}}{N^*_{nl}} \,. \tag{3.1}$$

A departure coefficient b_{nl} that is equal to unity indicates that the level nl is in LTE with the electron gas. In this scheme, the Saha-Boltzmann equation (2.34)

for hydrogen becomes

$$N_{nl} = b_{nl} N_{\rm e} N_{\rm p} \left(\frac{h^2}{2\pi m_{\rm e} k_{\rm B} T_{\rm e}} \right)^{3/2} (2l+1) \exp\left(\frac{\chi_{nl}}{k_{\rm B} T_{\rm e}} \right) . \tag{3.2}$$

Collisional processes within the plasma become more efficient than their radiative counterparts as the principal quantum number n of the level increases. Therefore, for each set of physical conditions there will be an $n = n^*$ where the collisional processes dominate completely and set up Boltzmann distributions with temperature $T_{\rm e}$ among the levels so that $b_{nl} = 1$ for $n \geq n^*$.

There will be a $n = n_{\rm c} < n^*$ where the collisional processes will be much faster than the radiative processes, but radiative effects are still evident. For $n_{\rm c} < n < n^*$, the angular momentum states are populated statistically according to

$$N_{nl} = \frac{2l+1}{n^2} N_n \, . \tag{3.3}$$

The departure coefficient, b_n, that represent the departure from LTE for an energy level n is defined as the weighted sum of the b_{nl}'s[1]

$$b_n = \frac{1}{n^2} \sum_{l=0}^{n-1} (2l+1) b_{nl} \, . \tag{3.4}$$

Therefore, it follows that $b_n = b_{nl}$ for $n > n_{\rm c}$.

For levels with $n \geq n_c$ the level populations can be accurately derived from the results of an n-model, where elastic collisions have set up Boltzmann distributions amongst the l-levels. Using an iterative method of solution (see section 3.4.1) to solve the nl-model, the results from the n-model with the same physical conditions serve as the initial conditions for the nl-model.

Goldberg (1966) introduced an amplification factor $\beta_{nn'}$ with $n > n'$ that is given by

$$\beta_{nn'} = \frac{\left(1 - \frac{b_{n'}}{b_n} e^{-h\nu/k_{\rm B}T_{\rm e}} \right)}{(1 - e^{-h\nu/k_{\rm B}T_{\rm e}})} \, . \tag{3.5}$$

[1]The notation "b_{nl}'s" indicates a plural, as opposed to a possesive.

The amplification factors give the departure of the ratios of level populations from what is expected in LTE, as opposed to the departure coefficients that represent the departure of individual level populations from LTE. A value of $\beta_{n,n'} < 0$ indicates a population inversion between levels n and n', with an increased amount of inversion for decreasing values of $\beta_{nn'}$. Therefore, stimulated emission will be important for levels for which $\beta_{nn'} \ll 0$. An illustrative discussion of the amplification factor can be found in Strelnitski et al. (1996a).

Baker & Menzel (1938) introduced two simple assumptions which are referred to as Case A and Case B. For Case A, the nebula is taken to be optically thin to all line radiation. For Case B, it is assumed that all photons produced by Lyman transitions are optically thick and are absorbed close to the point where they are emitted (this is called the on-the-spot approximation). From a calculational perspective, this means that all transitions to the $n = 1$ level are ignored. Osterbrock (1962) concluded that Case B is a good quantitative approximation for nebular conditions.

3.3 The n-model

The rates of the atomic processes are assumed to be much faster than the dynamical changes in the plasma, hence it is appropriate to assume that the plasma is stationary over time-scales that we observe it. The level populations N_n are described by statistical equilibrium so that the total rate of all transitions into any particular atomic level must equal the total rate of the transitions out that level.

The approach of Brocklehurst (1970) was followed for the n-model. In addition to the processes in the Brocklehurst model, my n-model includes stimulated emission and absorption terms. Assembling all the atomic processes occurring into and out

of level n gives the statistical balance equation

$$\begin{aligned} & N_\mathrm{e}N_\mathrm{p}\left(\alpha_n^\mathrm{r}+\alpha_n^\mathrm{s}+N_\mathrm{e}C_{i,n}\right)+\sum_{m>n}N_m\left(A_{mn}+N_\mathrm{e}C_{mn}+B_{mn}J_\nu\right) \\ & \qquad +\sum_{k<n}N_k\left(N_\mathrm{e}C_{kn}+B_{kn}J_\nu\right) \\ & =N_n\left[\alpha_n^\mathrm{p}+N_\mathrm{e}C_{n,i}+\sum_{k<n}\left(A_{nk}+N_\mathrm{e}C_{nk}+B_{nk}J_\nu\right)+\sum_{m>n}\left(N_\mathrm{e}C_{nm}+B_{nm}J_\nu\right)\right]. \end{aligned} \tag{3.6}$$

The left-hand side contains all processes that populate level n. The terms represent radiative recombination (α_n^r), stimulated recombination (α_n^s), three-body recombination ($C_{i,n}$), spontaneous emission ($A_{nn'}$), stimulated emission ($B_{nn'}$), collisional de-excitation ($C_{nn'}$) and absorption ($B_{n'n}$). The mean intensity of incident radiation fields is given by J_ν.

The right-hand side includes all processes that depopulate level n. The terms represent photoionisation (α_n^p), collisional ionisation ($C_{n,i}$), spontaneous emission, stimulated emission, collisional de-excitation, collisional excitation and absorption, respectively.

The departure coefficients b_n are related to the number density N_n of atoms in level n through the Saha-Boltzmann equation. Substituting this into the rate equation (3.6) yields

$$\begin{aligned} & \left(\frac{2\pi m_\mathrm{e}k_\mathrm{B}T_\mathrm{e}}{h^2}\right)^{3/2}\left(\alpha_n^\mathrm{r}+\alpha_n^\mathrm{s}+N_\mathrm{e}C_{i,n}\right)+\sum_{m>n}b_m m^2 e^{\chi_m/k_\mathrm{B}T_\mathrm{e}} \\ & \qquad \times\left(A_{mn}+N_\mathrm{e}C_{mn}+B_{mn}J_\nu\right)+\sum_{k<n}b_k k^2 e^{\chi_k/k_\mathrm{B}T}\left(N_\mathrm{e}C_{kn}+B_{kn}J_\nu\right) \\ & =b_n n^2 e^{\chi_n/k_\mathrm{B}T_\mathrm{e}}\left[\alpha_n^\mathrm{p}+N_\mathrm{e}C_{n,i}+\sum_{k<n}\left(A_{nk}+N_\mathrm{e}C_{nk}+B_{nk}J_\nu\right)\right. \\ & \qquad \left.+\sum_{m>n}\left(N_\mathrm{e}C_{nm}+B_{nm}J_\nu\right)\right]. \end{aligned} \tag{3.7}$$

In principle, an isolated atom has an infinite number of energy levels. To make the

mathematics computationally viable, an upper cut-off $n_{\max}$ is introduced for the highest n level for which the rate equations are solved explicitly. The contributions to the sums above $n_{\max}$ are converted into an integral using the trapezoidal rule. This integral is then approximated using a 20-point Gaussian quadrature. The remaining rate equations are cast into matrix form.

Because the departure coefficients vary smoothly and slowly with n, the Lagrange interpolation technique of Burgess & Summers (1969) is employed to reduce the number of equations to be solved five fold. A number of authors (e.g. Brocklehurst, 1970; Burgess & Summers, 1976; Storey & Hummer, 1995) have used this method, and it was once again found to compare very satisfactorily with the results of solving the full system of equations. The technique condenses the sizable matrix to a much smaller matrix, economising the amount of dynamic memory needed to perform the calculation and speeding up computation time considerably. The condensed rate equations are solved by direct Gaussian elimination with the use of partial pivoting. The resulting condensed vector containing the b_n values is interpolated to give the full set of values. The b_n values found using this method compare very well with the results of solving the full system of equations.

3.4 The nl-model

The rate equation for a level nl in the nl-model, similar to equation (3.7) that is solved for the n-model, is

$$\begin{aligned}
&\left(\frac{h^2}{2\pi m_\mathrm{e} k_\mathrm{B} T_\mathrm{e}}\right)^{-3/2} (\alpha^\mathrm{r}_{nl} + \alpha^\mathrm{s}_{nl} + N_\mathrm{e} C_{i,nl}) \; + \\
&\sum_{m>n} \sum_{l'=l\pm1} b_{ml'}(2l'+1) e^{\chi_{ml'}/k_\mathrm{B}T_\mathrm{e}} \left(A_{ml',nl} + B_{ml',nl} J_\nu + N_\mathrm{e} C_{ml',nl}\right) \\
&+ \sum_{k<n} \sum_{l''=l\pm1} b_{kl''}(2l''+1) e^{\chi_{kl''}/k_\mathrm{B}T_\mathrm{e}} \left(B_{kl'',nl} J_\nu + N_\mathrm{e} C_{kl'',nl}\right) \\
&+ \sum_{l'=l\pm1} b_{nl'}(2l'+1) e^{\chi_{nl'}/k_\mathrm{B}T_\mathrm{e}} \sum_q N_q C^q_{nl',\,nl} \\
&= \; b_{nl}(2l+1) e^{\chi_{nl}/k_\mathrm{B}T_\mathrm{e}} \Bigg[\alpha^\mathrm{p}_{nl} + N_\mathrm{e} C_{nl,i} \\
&+ \sum_{k<n} \sum_{l''=l\pm1} \left(A_{nl,kl''} + B_{nl,kl''} J_\nu + N_\mathrm{e} C_{nlkl''}\right) \\
&+ \sum_{m>n} \sum_{l'=l\pm1} \left(B_{nl,ml'} J_\nu + N_\mathrm{e} C_{nl,ml'}\right) \; + \sum_{l'=l\pm1} \sum_q N_q C^q_{nl,nl'} \Bigg] \; .
\end{aligned} \tag{3.8}$$

In equation (3.8) the elastic collision terms ($C^q_{nl,nl'}$) are included. The N_q represent the number densities of the different species interacting via elastic collisions with the bound electrons. In this work, electrons, protons and He^+ ions are taken to induce these collisions, with the proton number density $N_\mathrm{p} = 0.909 N_\mathrm{e}$ and the He^+ number density $N_{\mathrm{He}^+} = 0.090 N_\mathrm{e}$. These are the same values used as by SH95.

Equation (3.8) represents a system of linear equations in the b_{nl} values. Therefore, they can be written in matrix form as

$$\mathbf{A} \cdot \mathbf{b} = \mathbf{y} \tag{3.9}$$

where $\mathbf{b}$ is a vector with the b_{nl} values as entries. The diagonal entries of the matrix $\mathbf{A}$ represent the processes depopulating a level nl and the off-diagonal entries in a

given row are the bound-bound processes that are populating that level. The vector $\mathbf{y}$ contains the first term of equation (3.8) as well as the populating contributions of levels with $n > n_\mathrm{c}$.

The populating contributions of the first 20 energy levels beyond n_c are calculated explicitly and incorporated into the vector $\mathbf{y}$ in equation (3.9). The populating effects of levels $n > n_\mathrm{c}+20$ are approximated with a 20-point Gaussian quadrature in the same way as the contributions of $n > n_\mathrm{max}$ are handled in the n-model and added to $\mathbf{y}$. The depopulating effects of levels with $n_\mathrm{c} < n \leq n_\mathrm{c} + 20$ and $n > n_\mathrm{c}+20$ are treated similarly, but added to the total depopulation rate for each level contained in the diagonal of the matrix $\mathbf{A}$.

The level n_c is determined empirically to ensure the results of the nl-model are used up to a sufficiently high principal quantum number so that they match the results of the n-model to four significant digits. The level above which equation (3.4) is valid was found to be only weakly dependent on temperature, and mostly determined by the electron density. It is calculated using

$$n_\mathrm{c} = 350 - 15\ln(N_\mathrm{e})$$

and rounding up to the nearest multiple of 5.

To obtain the departure coefficients for $n \leq n_\mathrm{c}$, the rate equations (3.8) have to be solved simultaneously. The main difference between the b_n's from the n-model and the ones obtained from the nl-model and equation (3.4) is the inclusion of the elastic collisions between bound electrons and free particles. The elastic collisions' effects are important for the populations of mid- to high-energy levels where the b_n's calculated with the nl-model can differ significantly from those of the n-model.

Equation (3.9) represents a total of $n_\mathrm{c}(n_\mathrm{c}+1)/2$ equations that have to be solved simultaneously. This value is generally $\sim 10^4$. Because the values of b_{nl} do not vary smoothly, the matrix condensation technique used in the n-model cannot be employed at this step. The rate equations (3.9) of the nl-model can be solved using either an iterative method or a direct approach. The iterative solver was used initially and provides a straightforward way to explain the differences between the

current work and previous results. The iterative method is very time expensive and in practice a direct solver that could exploit certain properties of the system of linear equations is utilized.

3.4.1 Iterative solution method

An iterative method of solution is usually employed for systems of equations that contain a large number of equations and has been used extensively in previous departure coefficient calculations (e.g. Brocklehurst, 1971; Smits, 1991; Storey & Hummer, 1995; Salgado et al., 2017). The values of the b_{nl}'s for a specific set of conditions are found using a two step process. The procedure is a derivative of the Gauss-Seidel method and is described in Brocklehurst (1971). The same method was used by SH95 and Salgado et al. (2017).

First, an n-model for the same set of physical conditions is solved to obtain values for b_n. The values produced by this method are valid for $n > n_c$ where equation (3.3) holds. The departure coefficients b_n from the n-model are used as the initial values for the departure coefficients so that $b_{nl} = b_n$ at the start of the calculation. The rate equation (3.9) is then solved to obtain b_{nl} for decreasing values of n starting with $n = n_c$. The b_{nl} values for a given n are solved simultaneously as an $n \times n$ matrix by including all the terms that do not depend on these specific b_{nl} values in the right-hand side of equation (3.9). Each newly calculated set of b_{nl}'s is used in subsequent calculations down to $n = 2$ for Case A and $n = 3$ for Case B. This constitutes one iteration and the process is repeated multiple times with increasingly accurate values for the b_{nl}'s until they converge to an accuracy of 4 decimal digits.

Stopping criterion

An important aspect of an iterative solution is a test to indicate when convergence of the departure coefficients has been achieved, and to stop the iterations. In most previous work, the stopping criterion has not been explicitly stated, except for

Salgado et al. (2017), who terminate their iterative procedure when the difference between two successive iterations is less than 1 per cent. I show here that such a stopping criterion is not appropriate and can stop the iterative process before the values of the departure coefficients have converged to values within a known error.

If the iterative procedure is making small corrections to the b_{nl}'s, the convergence rate can be slow, with the result that a stopping criterion such as the one used by Salgado et al. (2017) can signal convergence has occurred. Many more iterations can be required before convergence is reached. These tiny corrections can accumulate to a significant number, as will be shown below. For the conditions considered in this work, the matrix $\mathbf{A}$ has a condition number $\kappa(\mathbf{A}) \sim 10^7$ which is very large and means the matrix is ill-conditioned, which results in a slow convergence rate (Douglas et al., 2016). The condition number is defined later in the chapter.

To derive a stopping criterion, I define the following quantities and notation. Let $\mathbf{b}^{(i)}$ be the vector containing the departure coefficients as entries after i iterations. The residual $\mathbf{r}^{(i)}$ after i iterations is given by

$$\mathbf{r}^{(i)} = \mathbf{A}\cdot\mathbf{b}^{(i)} - \mathbf{y} \tag{3.10}$$

and provides an indication of the quality of $\mathbf{b}^{(i)}$. The vector of errors $\mathbf{e}^{(i)}$ after i iterations is the difference between $\mathbf{b}^{(i)}$ and the true solution $\mathbf{b}$, i.e.

$$\mathbf{e}^{(i)} = \mathbf{b}^{(i)} - \mathbf{b}\,. \tag{3.11}$$

Of course, $\mathbf{b}$ is generally unknown and therefore $\mathbf{e}^{(i)}$ cannot be calculated directly. However, if an upper bound for the error can be defined then a stopping criterion can be constructed such that the iterations will only stop after it is guaranteed that the errors are smaller than some predefined number.

A norm of a vector or matrix, indicated using double bars $\|\cdot\|$, is a non-negative number that gives a measure of the magnitude of the vector or matrix. There are various types of norms that can be defined, all of which obey a specified set of

properties. In particular, for a matrix $\mathbf{M}$ and vector $\mathbf{v}$ the inequality

$$\|\mathbf{M}\mathbf{v}\| \leq \|\mathbf{M}\|\|\mathbf{v}\| \tag{3.12}$$

will hold for any consistent pair of vector and matrix norms. Note that the quantity called the condition number mentioned above is defined as

$$\kappa(\mathbf{M}) = \|\mathbf{M}^{-1}\| \, \|\mathbf{M}\| \, . \tag{3.13}$$

If $\kappa(\mathbf{M}) \gg 1$ then the matrix is called ill-conditioned.

Using the tools developed above, an appropriate stopping criterion for an iterative solution to the set of equations represented by equation (3.9) can now be derived. Substituting equation (3.9) into equation (3.11) and using equation (3.10) gives

$$\begin{aligned} \mathbf{e}^{(i)} &= \mathbf{b}^{(i)} - \mathbf{A}^{-1}\mathbf{y} \\ &= \mathbf{A}^{-1}(\mathbf{A}\cdot\mathbf{b}^{(i)} - \mathbf{y}) \\ &= \mathbf{A}^{-1}\mathbf{r}^{(i)}. \end{aligned} \tag{3.14}$$

Taking the norm on both sides and using the submultiplicative property given in equation (3.12) leads to

$$\|\mathbf{e}^{(i)}\| = \|\mathbf{A}^{-1}\mathbf{r}^{(i)}\| \leq \|\mathbf{A}^{-1}\|\|\mathbf{r}^{(i)}\| \, . \tag{3.15}$$

Therefore, stopping the iterative procedure only after

$$\|\mathbf{r}^{(i)}\| \leq \epsilon \cdot \frac{\|\mathbf{b}^{(i)}\|}{\|\mathbf{A}^{-1}\|} \tag{3.16}$$

will guarantee that the relative error is smaller than some predefined tolerance $\epsilon \ll 1$. That is, equation (3.16) implies

$$\frac{\|\mathbf{e}^{(i)}\|}{\|\mathbf{b}^{(i)}\|} \leq \frac{\|\mathbf{A}^{-1}\|\|\mathbf{r}^{(i)}\|}{\|\mathbf{b}^{(i)}\|} \leq \epsilon \, . \tag{3.17}$$

Equation (3.17) is true for any consistent pair of vector and submultiplicative matrix norms.

One appropriate set of such norms is the l_1 norm of a vector and the corresponding operator norm of a matrix. For a general n-vector $\mathbf{v}$ with components v_i and a general $n \times n$ matrix $\mathbf{M}$ with entries m_{ij}, these norms are given respectively by

$$\|\mathbf{v}\|_1 = \sum_{i=1}^{n} |v_i| \qquad \text{and} \qquad \|\mathbf{M}\|_1 = \max_{1 \leq j \leq n} \sum_{i=1}^{n} |m_{ij}| \; . \tag{3.18}$$

The matrix norm $\|\mathbf{M}\|_1$ corresponds to the maximum sum of the absolute values of the individual columns of $\mathbf{M}$.

The calculation of matrix inverses is notoriously expensive. Because an algorithm for estimating the l_1 norm of the inverse of a matrix is available, these norms have been used. The algorithm of Hager (1984) that estimates the l_1 norm of the inverse of a matrix without inverting the matrix first, was refined by Higham (1988). This algorithm usually gives the exact value of $\|\mathbf{A}^{-1}\|_1$ and, at worst, gives an order of magnitude estimate for the types of matrices considered here (Higham, 1988). The values of $\|\mathbf{b}^{(i)}\|_1$ and $\|\mathbf{r}^{(i)}\|_1$ can be calculated directly.

3.4.2 Direct solution method

It will be shown in section 4.1 that the iterative method can require a large number of steps ($\sim \mathcal{O}(10^5)$) before convergence is reached, which can take a significant amount of time. The matrix $\mathbf{A}$ is large, but because only dipole transitions have been included in the model, $\mathbf{A}$ is sparse, i.e. most of the entries in the $\mathbf{A}$ matrix are equal to zero.

Obtaining a solution from thousands of iteration steps takes a significant amount of time. To speed up the solution, a direct solver using the PARDISO[2] package (Petra et al., 2014a,b) was tested. It is a sophisticated solver for systems of linear

[2] `http://pardiso-project.org`

equations that exploits the sparsity of $\mathbf{A}$ to solve the system in a very efficient manner. The direct solver is considerably faster at solving the set of linear equations than the iterative method.

The departure coefficients shown in Chapter 4 were obtained using the above direct solver package. The b_{nl}'s obtained from the iterative method with the given stopping criterion match those using the direct solver. An error estimate of the quality of the results of the direct solver was obtained using

$$\epsilon \approx \|\mathbf{A} \cdot \mathbf{b} - \mathbf{y}\| / \|\mathbf{b}\| \,. \tag{3.19}$$

It was found that $\epsilon \leq 10^{-4}$ in all cases.

3.5 Consistency tests

A number of self-consistency checks were performed on both the n- and nl-models. These consist of setting up extreme conditions where the level populations are expected to be in Boltzmann distributions and all departure coefficients should therefore be equal to unity.

The free particles are assumed to be in LTE with each other, so the collisional processes should set up Boltzmann distributions between the level populations. All processes were turned off except collisional processes of a certain type (bound-free, bound-bound or angular momentum changing for the nl-model). This condition was met exactly except for the bound-free collisional processes of the nl-model where the results are accurate to four significant digits. This is due to the assumption that the bound-free collisional cross-sections are independent of the angular momentum quantum number, i. e. $C_{nl,i} = C_{n,i}$.

A further test was to turn the collisions off and set $J_\nu = B_\nu\left(T_\mathrm{r}\right)$. It is expected that all departure coefficients will be equal to unity if $T_\mathrm{e} = T_\mathrm{r}$. This was found to be the case for both bound-bound and bound-free processes.

Chapter 4

C^3 model results

4.1 Effects of the new stopping criterion

In this section an iterative procedure is applied to the system of linear equations (3.9) in order to show the effect of the stopping criterion given in equation (3.16) on the departure coefficients. Previous authors have not paid much attention to the stopping criterion of their iterative procedures to solve for the departure coefficients. A condition typically applied to terminate the algorithm is when the difference between two successive iterations changes by a small amount. This condition may not give accurate results if the convergence rate is slow, as in the case with departure coefficient calculations.

Initially, a standard Gauss-Seidel iterative method was used to solve the system of equations (3.9). In this method the b_n's obtained from the n-model are used as initial values, so that $b_{nl} = b_n$. The rate equation (3.8) is then solved to obtain each b_{nl} for decreasing values of n and l starting with $n = n_c$ and $l = n_c - 1$. Each newly calculated value of b_{nl} is used in subsequent calculations.

Fig. 4.1 shows the evolution of a subset of departure coefficients as the Gauss-Seidel iterative procedure progresses for a gas at $T_e = 10^4$ K with density $N_e = 10^4\,\mathrm{cm}^{-3}$ for Case B with no external radiation field present. The values on the left-hand side of the graph show the values after one iteration, with the n-model results for

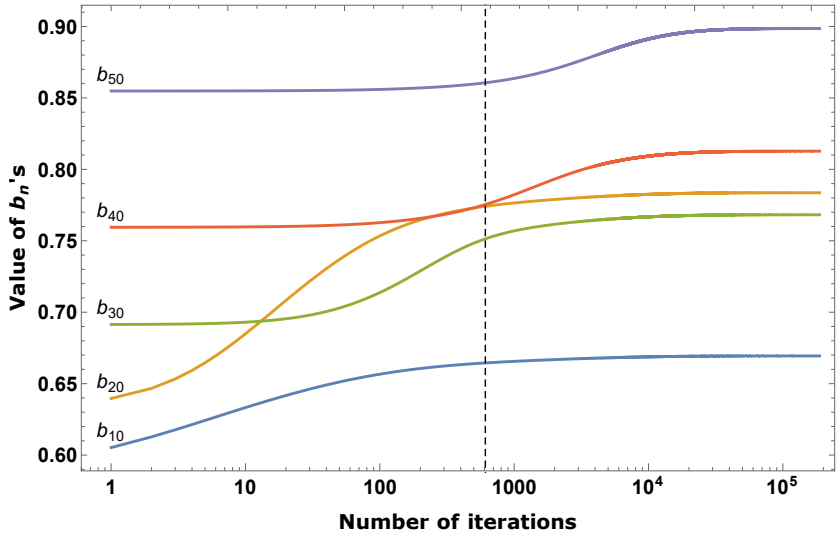

Figure 4.1 – The evolution of five departure coefficients for $T_e = 10^4$ K, $N_e = 10^4$ cm^{-3} Case B as the standard Gauss-Seidel iterative procedure of the nl-model progresses. The b_n values, determined by equation (3.4), are shown for different values of n. Convergence is reached after 187 632 iterations. The dashed line at 610 iterations shows the first point where the values of the b_{nl}'s change by less than 1 per cent for two successive iterations.

the same physical conditions used as starting values. The values plotted are the b_{nl} values summed over l as given in equation (3.4). The values on the far right indicate the values after convergence is reached using equation (3.16). For this case, the b_{nl}'s converged to four significant digits ($\epsilon = 5 \times 10^{-5}$) after 187 632 iterations. The dashed vertical line at 610 iterations indicates the first point in the process where the all departure coefficients b_{nl} from two successive iterations change by less than 1 per cent. From the graph it is clear that a small change in the departure coefficients during the procedure is not sufficient to indicate convergence.

In an effort to reduce the computation time of the programme, the Gauss-Seidel method was modified so that all b_{nl}'s for each value of n were solved simultaneously as described in section 3.4.1. This reduced the iterations required to reach convergence by a few orders of magnitude. A graph comparable to Fig. 4.1 using this improved method is shown in Fig. 4.2. In this case convergence was reached after 1 375 iterations and the departure coefficients started to change by less than

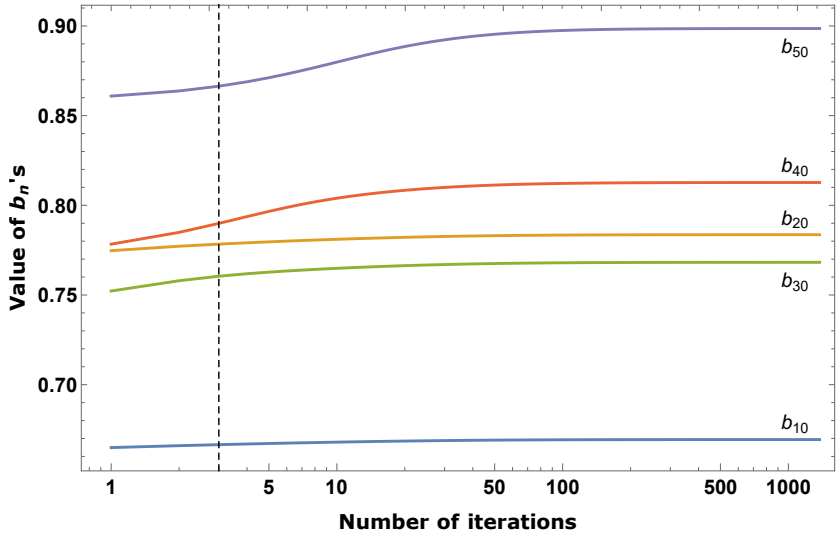

Figure 4.2 – The evolution of five departure coefficients for $T_e = 10^4\,\mathrm{K}$, $N_e = 10^4\,\mathrm{cm}^{-3}$ Case B as the improved iterative procedure of the nl-model progresses. Convergence is reached after 1 375 iterations. The dashed line at 3 iterations shows the first point where the values of the b_{nl}'s change by less than 1 per cent.

1 per cent after only 3 iterations.

Fig. 4.3 shows the departure coefficients for $T_e = 10^4\,\mathrm{K}$, $N_e = 10^4\,\mathrm{cm}^{-3}$ Case B as calculated from different models. The n-model results (green line) is used as a starting value for the more sophisticated nl-model presented in this work (blue line). The results of SH95 is shown as the yellow line and can be obtained by terminating the current model before full convergence as described equation (3.16) by has been reached. Comparing this figure to Figs. 4.1 and 4.2 shows how the departure coefficients for lower n-levels converge first, and those of higher n-levels later as the iterative procedure progresses. A more detailed discussion between the current results and those of SH95 is given in section 4.2.

4.2 Comparison to previous results

A comparison of the current results with those of SH95 for a range of temperatures at a fixed electron density of $N_e = 10^4\,\mathrm{cm}^{-3}$ is shown in Fig. 4.4. The largest

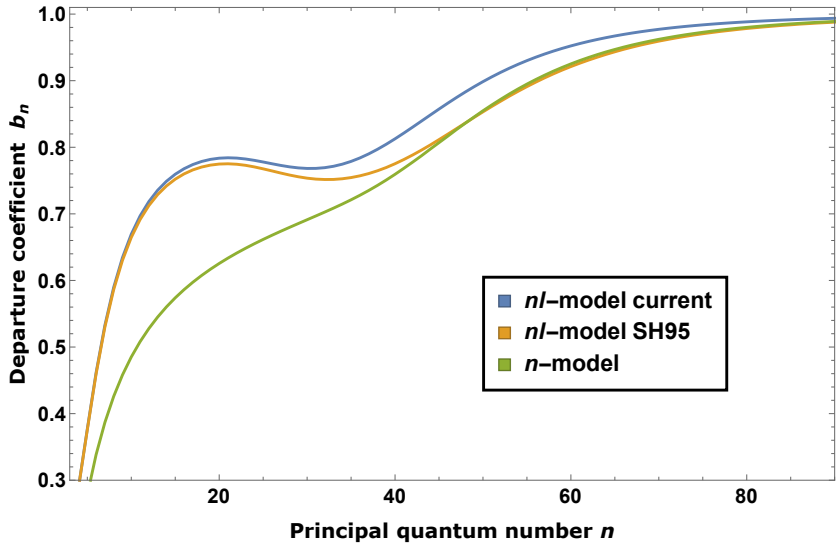

Figure 4.3 – Comparison between the departure coefficients of the n-model (green line), the current nl-model (blue line) and the nl-model of SH95 (yellow line) for $T_e = 10^4$ K, $N_e = 10^4$ cm^{-3} Case B. The b_n values from the nl-models were determined by equation (3.4).

discrepancy occurs at intermediate principal quantum numbers. This is unsurprising, since the behaviour of the b_{nl}'s at low and high n's are not governed by the nl-model. At low energy levels, radiative processes dominate and the departure coefficients would be largely unaffected by the elastic collisions introduced in the nl-model. Therefore, at these levels the final b_{nl}'s will be very close to their initial values obtained from the n-model. At high energy levels, the collisional processes dominate completely and all b_{nl}'s will tend towards unity, reducing the difference between the two sets of calculations.

Fig. 4.5 shows the difference between the unsummed b_{nl} values of SH95 and the current work. As expected, the differences are very small for low values of n, but become more pronounced as n and l increase. This effect is due to elastic collisions becoming the dominant process at intermediate and high n levels. The $l = 1$ state of each n-level depopulates faster than the other l-states and generally has the lowest population in each n-level. The spontaneous emissions out of an l-level are fastest for low values of l. However, the $l = 0$ level can only depopulate to lower levels with $l' = 1$ via spontaneous emissions, whereas the $l = 1$ state depopulates

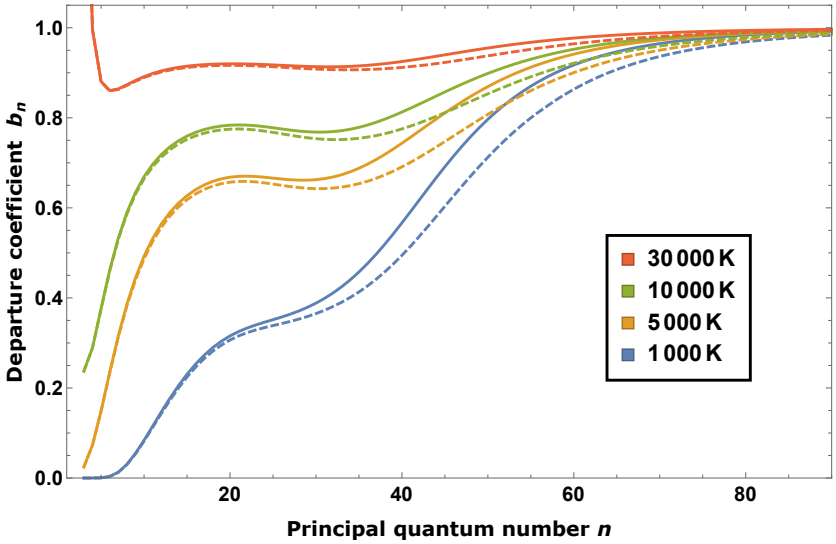

Figure 4.4 – Departure coefficients b_n for Case B for a variety of temperatures at electron density $N_\mathrm{e} = 10^4\,\mathrm{cm}^{-3}$. Dashed lines represent the values obtained by SH95 and solid lines in the same colour show the current results for the same conditions.

to both $l' = 0$, 2.

The results show that line enhancement of H$n\alpha$ transitions by stimulated emission for intermediate n are less extreme than previously thought, with the point of maximum inversion occurring at a lower level than in the SH95 results. Fig. 4.6 illustrates the amplification factor as defined in equation (3.5) for H$n\alpha$ transitions for the same parameters as Fig. 4.4. The lines that fall in the optical range are largely unaffected, with the largest deviation from previous results in the radio regime.

The discrepancy between my values and those of SH95 increases as the temperature decreases and the density increases; there is a stronger dependence on temperature than density. For $T_\mathrm{e} = 500\,\mathrm{K}$ and $N_\mathrm{e} = 10^6\,\mathrm{cm}^{-3}$ the maximum relative difference is 22.5 per cent. I can match the values of SH95 within a per cent by terminating my procedure prematurely. Storey (private communication) has noted that the SH95 model converges extremely fast (within 10 iterations) and that the departure coefficients do not change significantly if either the number of iterations or n_c is increased.

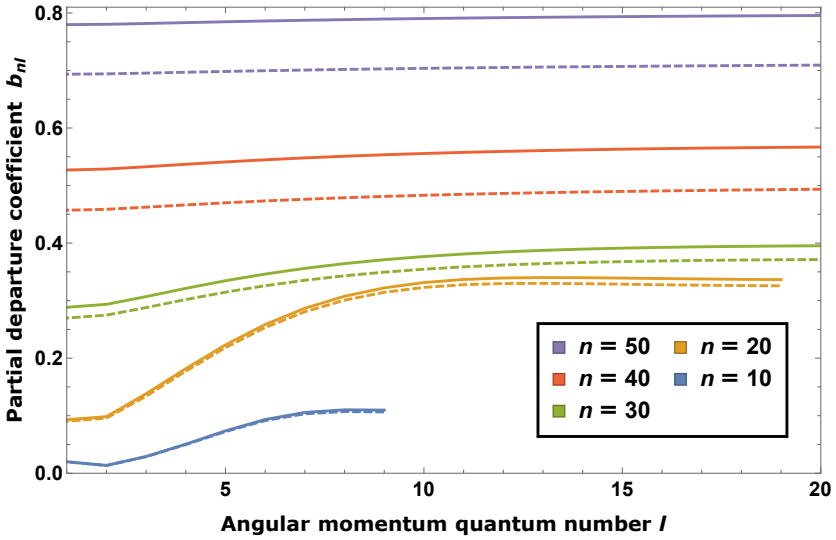

Figure 4.5 – Partial departure coefficients b_{nl} for a selected number of principal quantum numbers n for $T_\mathrm{e} = 10^3\,\mathrm{K}$ and $N_\mathrm{e} = 10^4\,\mathrm{cm}^{-3}$, Case B. Solid lines represent the calculations of this work, dashed lines of the same colour show the results of SH95 for the same n.

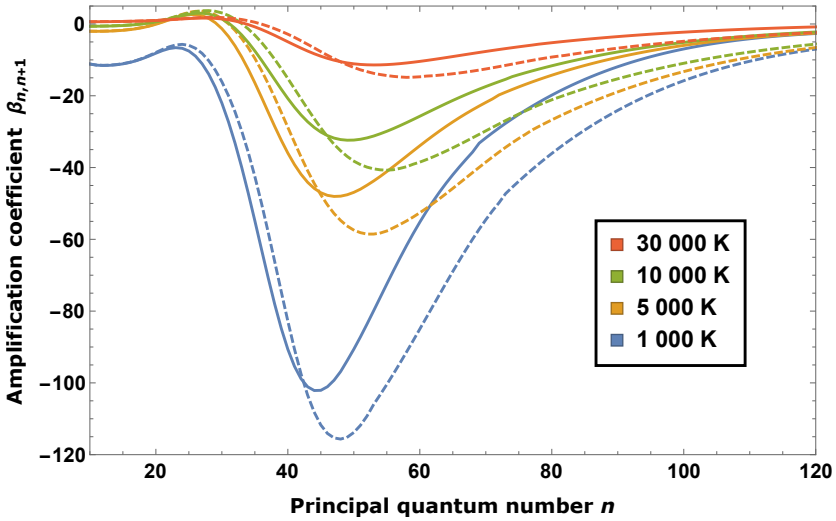

Figure 4.6 – The amplification factor $\beta_{n,n+1}$ for H$n\alpha$ transitions for electron density $N_\mathrm{e} = 10^4\,\mathrm{cm}^{-3}$ and a range of temperatures under Case B conditions. Solid lines show the current results and dashed lines are those of SH95.

At this stage I do not understand the reasons that the SH95 model converges so fast and to different values than mine. The differences in inelastic collisional rates between the models certainly plays a role, but does not account fully for the differences. I have performed many tests on my model, but cannot get it to converge as fast or to the same values as SH95. Clearly, this is an issue that needs further investigation.

4.3 Stimulating effects of continuum radiation

In this section I examine the effects of the continuum radiation fields on the population structure of hydrogen in nebular environments. Specifically, their role in stimulating transitions between excited states.

The continuum radiation in the diffuse ISM consists of different components, each of which are examined to determine their effect on departure coefficients. The radiation fields considered here are the stellar radiation field, the cosmic microwave background radiation (CMBR), the free-free radiation field generated by the electrons in the gas and emission from dust.

Fig. 4.7 shows the mean intensity J_ν of these fields as a function of the frequency associated with H$n\alpha$ transitions. The population inversion of the bound electrons in excited states is most pronounced for energy levels $30 \lesssim n \lesssim 80$ (cf. Fig. 4.6), so that electrons in these levels are susceptible to being stimulated.

4.3.1 Stellar radiation field

Photoionised nebulae require a nearby hot source of ultraviolet radiation to ionise atoms in the gas. In Fig. 4.7 the blackbody radiation field from a $T = 50\,000\,\mathrm{K}$ source with dilution factor $W = 10^{-12}$ is shown on the far left. For a single ionizing star with a radius of R, the dilution factor at a distance d from the star will be

$$W \approx \frac{1}{4}\left(\frac{R}{d}\right)^2 \quad \text{for} \quad d \gg R\,.$$

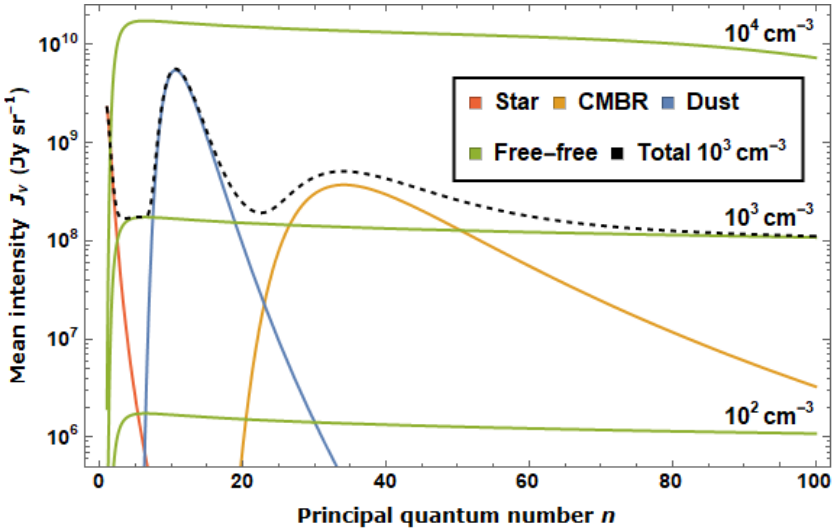

Figure 4.7 – Spectrum of continuum radiation fields J_ν within a model ionised nebula at $T_\mathrm{e} = 10^4\,\mathrm{K}$. The free-free field is shown for three different densities. The horizontal axis shows the principal quantum number for H$n\alpha$ transitions, and the vertical axis shows the mean intensities of the various radiation fields.

For an O star with $R = 18R_\odot$, the dilution factor is $W \sim 10^{-12}$ at $d = 40\,\mathrm{AU}$. As can be seen, the intensity of the ionising radiation from such a hot star drops off very quickly with decreasing frequency (increasing n in the diagram) and is negligible at frequencies low enough to stimulate transitions in hydrogen. An O or B star has to be a distance of $\lesssim 10\,\mathrm{AU}$ from the gas to have any noticeable effect on the departure coefficients and, therefore, can be neglected in these calculations.

4.3.2 Cosmic microwave background radiation

The CMBR has a low temperature ($T = 2.7\,\mathrm{K}$) but is undiluted blackbody radiation. Coincidentally, the intensity of the radiation peaks around a frequency corresponding to H$n\alpha$ with $n \sim 40$ which is where the population inversion is strongest.

For a density of $N_\mathrm{e} = 10^2\,\mathrm{cm}^{-3}$ stimulated emissions due to the CMBR make up in excess of 10 per cent of the downward H$n\alpha$ transitions for $40 \lesssim n \lesssim 60$. As the

density increases, the effect of stimulated emission decreases because the influence of elastic collisions increases at these levels. The correction that the inclusion of the CMBR in the model provides to the summed b_{nl}'s is typically less than 1 per cent.

4.3.3 Free-free radiation

Continuous free-free radiation is produced by a plasma as charged free particles interact with each other without capture taking place. The free particles of opposite charge are assumed to be in thermodynamic equilibrium at a temperature T_e. Disregarding background radiation, the specific intensity of the free-free radiation is given by

$$J_\nu^\mathrm{ff} = B_\nu(T_\mathrm{e}) \left(1 - e^{-\tau_\nu^\mathrm{ff}}\right) , \tag{4.1}$$

where B_ν is the Planck function for frequency, and τ_ν^ff is the optical depth of this radiation.

Following Dickinson et al. (2003), the appropriate optical depth for the free-free radiation is given by

$$\begin{aligned} \tau_\nu^\mathrm{ff} = {} & 3.014 \times 10^{-2}\, T_\mathrm{e}^{-3/2} \left(\frac{10^9}{\nu}\right)^2 \\ & \times \left[\ln\left(4.955 \times 10^{-2}\nu^{-1}\right) + 1.5 \ln\left(T_\mathrm{e}\right)\right] (\mathrm{EM}) , \end{aligned} \tag{4.2}$$

where $\mathrm{EM} = \int N_\mathrm{e}^2\, ds$ is the emission measure in $\mathrm{cm}^{-6}\,\mathrm{pc}$. For a homogeneous gas, $\mathrm{EM} = N_\mathrm{e}^2\,\mathrm{cm}^{-6}\,\mathrm{pc}$.

The intensity of the free-free radiation within a nebula is strongly dependent on the electron density N_e. The effect of this radiation on the population structure of hydrogen is negligible for low densities, but can become significant for $N_\mathrm{e} > 10^4\,\mathrm{cm}^{-3}$. For example, the departure coefficients of a gas with $N_\mathrm{e} = 10^6\,\mathrm{cm}^{-3}$ and $T_\mathrm{e} = 10^4\,\mathrm{K}$ will be affected by up to 12 per cent around $n = 20$ by the inclusion of the free-free radiation field due to stimulated processes, as illustrated in Fig. 4.8. The relative difference as shown in the figure is defined as $\left(b_n^\mathrm{ff} - b_n^0\right)/b_n^0$,

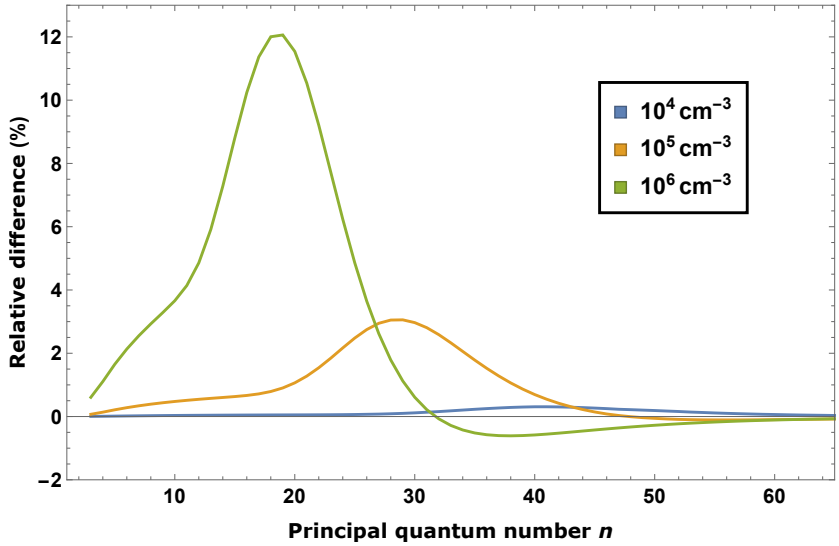

Figure 4.8 – The effects of the free-free radiation field on the population structure of hydrogen for $T_e = 10^4$ K, and a range of densities in Case B. The relative difference between the departure coefficients calculated when no radiation field is present and when the free-free field is included in the calculations are shown for each principal quantum number.

where $b_n^{\rm ff}$ represents the departure coefficients with free-free radiation included in the model and b_n^0 the values where no external radiation is included. The free-free radiation affects departure coefficients for principal quantum numbers in the range $10 \lesssim n \lesssim 60$.

4.3.4 Dust

Dust grains form an important component of the ISM and have been found to be intermixed with the ionised media of HII regions and planetary nebulae (Barlow, 1993; Kingdon & Ferland, 1997). Emission from dust grains can dominate the spectrum from HII regions and PNe at long wavelengths, outshining the free-free specific intensity by orders of magnitudes.

To model the emission from dust within the cloud, a modified blackbody spectrum of the form

$$J_\nu^{\rm d} = \tau_\nu^{\rm d} B_\nu(T_{\rm d})\,, \tag{4.3}$$

is used, where τ_ν^{d} is an optical depth and T_{d} is the dust temperature (Planck Collaboration et al., 2014). The angle-averaged optical depth

$$\tau_\lambda^{\mathrm{d}} = 1.5 \times 10^{-3} \left(\frac{100\,\mu\mathrm{m}}{\lambda} \right)^{1.7} \quad \Longleftrightarrow \quad \tau_\nu^{\mathrm{d}} = 9.2362 \times 10^{-25} \nu^{1.7} \tag{4.4}$$

from Draine (2011) is used.

The effect of the dust radiation on the b_n values is very limited as the populations are only weakly inverted at the frequencies where this radiation can stimulate transitions. In Fig. 4.7 a dust temperature of $T_{\mathrm{d}} = 50\,\mathrm{K}$ (Dupac et al., 2003) is shown, but the result is independent of T_{d} since this has little effect on the frequency range of the field.

In this work I have only considered the effect of the radiation from dust on the level populations. Hummer & Storey (1992) have shown that absorption by dust can affect the Case B recombination spectrum, possibly with a greater effect on the departure coefficients than emission.

4.4 Published tables

The programme described here calculates departure coefficients b_{nl} for level nl in hydrogen. From this, theoretical spectral line intensities can be calculated. The formulae required to calculate values that can be compared with observed lines are presented below, and then the entries in the tables are explained.

The tables containing my results are available online in machine-readable ASCII format and can be downloaded from the article webpage of Prozesky & Smits (2018) (`https://academic.oup.com/mnras/article/478/2/2766/4993330`). The file names are a concatenation of the significands and exponents of the electron density and temperature, the case (A or B) and any ambient radiation that has been included in the model, all separated by an underscore. Free-free radiation is indicated by 'FF', the CMBR by 'CMB', and no radiation field is designated with

Table 4.1 – An extract of one of the output tables for the conditions $T_e = 10^4$ K and $N_e = 10^4\,\mathrm{cm}^{-3}$, Case B, with no external radiation present. The values of the departure coefficients (b_n), the partial departure coefficients (b_{nl}), the emission coefficients ($j_{nn'}$) and the absorption coefficients ($\kappa_{n'n}$) are tabulated for each case.

```
NE = 10000 TE = 10000 CASE B NC = 210 NO RAD
---------------------------------------------
BN'S
 3   2.374e-01    4    2.895e-01    5    3.769e-01    6   4.616e-01    7   5.328e-01    8   5.897e-01    9   6.344e-01   10   6.694e-01   11   6.968e-01   12   7.184e-01
13   7.355e-01   14    7.489e-01   15    7.595e-01   16   7.678e-01   17   7.741e-01   18   7.787e-01   19   7.818e-01   20   7.836e-01   21   7.842e-01   22   7.838e-01
 ⋮
BNL'S
n = 3
 0   1.022e+00    1    2.336e-01    2    8.271e-02
n = 4
 0   1.132e+00    1    3.300e-01    2    1.446e-01    3   2.553e-01
n = 5
 0   1.206e+00    1    3.973e-01    2    1.891e-01    3   3.235e-01    4   4.239e-01
 ⋮
JNM'S
n = 4
 1   1.217e-25    2    9.879e-27    3    3.289e-27
n = 5
 1   5.304e-26    2    4.633e-27    3    1.602e-27    4   7.710e-28
n = 6
 1   2.830e-26    2    2.563e-27    3    8.903e-28    4   4.426e-28    5   2.432e-28
 ⋮
KMN'S
n = 4
 3   3.271e-23
n = 5
 3   1.003e-23    4   -8.418e-25
n = 6
 3   4.463e-24    4    2.892e-24    5   -1.518e-23
 ⋮
```

the number '0'. For example, the file named '13_14_B_0.dat' contains the results for Case B with $N_e = 10^3\,\mathrm{cm}^{-3}$ and $T_e = 10^4$ K with no ambient radiation present. The header in each file contains the same data as in the file name, as well as the value of n_c.

Each file contains the b_n values calculated using equation (3.4) for each value of n from $n = 2$ for Case A and $n = 3$ for Case B to $n = 500$. This is followed by the partial departure coefficients b_{nl} with the appropriate values of l tabulated after each value of n up to $n = 100$. The emission coefficients $j_{nn'}$ and absorption coefficients $\kappa_{n'n}$, as defined by equations (2.37) and (2.39), respectively, are given next. The coefficients are tabulated next to the lower level n' for ascending values of the upper level n. An extract of one of the data files is shown in Table 4.1.

Chapter 5

Hydrogen recombination line masers

5.1 Background

5.1.1 Hydrogen recombination line masers

Astronomical masers occur when spectral lines are amplified through stimulated emissions, and are observed to be much brighter than expected under LTE conditions. Molecular astronomical masers have been a very useful tool to probe conditions in a wide variety of sources such as star-forming regions, stellar atmospheres, shock excited nebulae associated with supernova remnants and in active galactic nuclei, whereas recombination line masers of hydrogen have been discovered in only a handful of objects. Traditional masers are produced by rotational or vibrational transitions in various molecules, whereas hydrogen recombination line (HRL) masers are due to transitions of excited electrons in atomic hydrogen.

Goldberg (1966) showed that recombination lines are amplified by stimulated emissions in the Rayleigh-Jeans limit, even at low optical depths. The theoretical possibility of HRL masers was considered by Krolik & McKee (1978) to account for the anomalous hydrogen line intensities found in dense gasses associated with active galactic nuclei. The first cosmic high-gain HRL maser was discovered in the young stellar object MWC 349A (Martin-Pintado et al., 1989a,b). This maser source has

since been studied extensively (Planesas et al., 1992; Thum et al., 1992, 1994a,b; Gordon, 1994; Martin-Pintado et al., 1994; Ponomarev, 1994; Thum et al., 1998; Gordon et al., 2001; Weintroub et al., 2008) confirming the presence of strongly masing HRLs.

For some time, MWC 349A was the only source in which HRL masers had been detected, but growing interest in the subject has prompted more searches, leading to the identification of a number of HRL masers in other objects. Masing HRLs have been observed in η Carinae (Cox et al., 1995), in a high-velocity ionised jet from the star-forming region Cepheus A HW2 (Jiménez-Serra et al., 2011), from the ultra-compact HII region Mon R2 (Jiménez-Serra et al., 2013), in the planetary nebula Mz 3 Aleman et al. (2018), in the gas surrounding the B[e] star MWC 922 (Sánchez Contreras et al., 2017) and toward the protostar G45.47+0.05 (Zhang et al., 2019). Because of anomalous H30α line emission, Murchikova et al. (2019) suggest the presence of an HRL maser in the accretion disc around the central Galactic black hole Sgr A*. The first extragalactic HRL maser has been detected in the star-forming galaxy NGC 253 (Báez-Rubio et al., 2018). The prospects of using HRL masers on cosmological scales to study the first galaxies (Rule et al., 2013) or the epoch of recombination and reionisation (Spaans & Norman, 1997) have been considered.

The environments in which these atomic masers can form are distinctly different from those of their molecular counterparts. For recombination lines to form, the emitting gas has to be ionised and for hydrogen this generally requires a temperature of $\sim 10^4$ K. This is a typical temperature of a photoionized nebula (Osterbrock & Ferland, 2006), which will be the focus of this work. Collisionally ionized gasses can have significantly higher electron temperatures. The host clouds of molecular masers are necessarily cooler than the molecule's dissociation temperature, and therefore are relatively cool and most of the hydrogen will be in molecular form. A population inversion occurs in hydrogen over a several decades of n-levels in a recombination nebula, whereas in molecular masers the inversion is often limited to one or at most a few levels. A result of this is that many adjacent HRL lines will exhibit masing behaviour at the same time instead of just a few specific lines as is the case with molecules. In HRL masers, the pumping scheme for the popu-

lation inversions is a natural consequence of the capture-cascade processes in the atomic component of an ionised gas, which is discussed in more detail in Strelnitski et al. (1996a). In many molecular masers the details associated with the pumping scheme are unclear. It should also be noted that because hydrogen makes up the bulk of almost all astronomical gasses, the masing species can be seen in very high densities in the case of hydrogen. For molecular masers the relevant constituents have low number densities compared to the H_2 content.

5.1.2 Challenges of maser modelling

Modelling the interaction between line photons and the emitting matter in an astronomical cloud is key to understanding masers. Such a model will have to account for not only the recombination theory and line formation in multi-level atoms, but also deal with the radiative transfer of the line photons through the cloud. A complete and simultaneous description of both of these components is a complex problem.

A C^3 model, such as the one described in Chapter 3, accounts for the influence that radiation has on atoms in an astronomical cloud by solving the statistical balance equations (SBE) for the level populations of hydrogen. This type of model is appropriate when the plasma is optically thin. When maser action is present, the line radiation is not optically thin and radiative transfer effects have to be accounted for. The ERT contains the effects that the matter has on the radiation field as it travels through the medium. However, the coefficients in the ERT depend on the local level populations, and the level populations in turn are influenced by the intensity of the radiation field, which is a non-local quantity. This means that these two effects are coupled to one another and, in principle, have to be solved simultaneously in a self-consistent manner to obtain the theoretical intensities of the spectral lines escaping the cloud. Simplifying assumptions, such as the escape probability approximation (EPA) discussed in section 5.3, are often employed to make the problem tractable.

Hydrogen masers are simpler than molecular masers in the extent that the cal-

culations include all relevant atomic processes to create population inversions. However, hydrogen masers are more complex to model in the sense that several atomic levels that interact directly with one another exhibit masing at the same time. The maser action in hydrogen therefore has a complex effect on the level populations of the participating levels.

5.1.3 Previous models of HRL masers

There have been some endeavours to construct a theoretical framework for HRL masers. Walmsley (1990) extended the departure coefficient calculations of Brocklehurst & Salem (1977b) to higher densities in response to the discovery of the first HRL masing region. Strelnitski et al. (1996a) addressed the theoretical foundations of HRL masers and considered conditions necessary for their formation.

Most theoretical models for HRL masers have focused on the morphology of the emitting region (e.g. Ponomarev et al., 1994; Strelnitski et al., 1996b; Weintroub et al., 2008) and it has been suggested that the masing is strongly related to the structure and kinematics of the emitting gas (Martín-Pintado, 2002). Most notable is the three-dimensional non-LTE radiative transfer code MORELI (Báez-Rubio et al., 2013). MORELI uses pre-calculated departure coefficients of either Walmsley (1990) or Storey & Hummer (1995), but does not solve the SBE in a self-consistent way.

Hengel & Kegel (2000) incorporated radiative transfer effects into a C^3 model to assess the effects of saturation on the level populations. They employed an n-model which neglects the effects of the elastic collisions between angular momentum states, as opposed to an nl-model in which they are included. Hengel & Kegel (2000) found that the effects of the radiative transfer on the level populations of hydrogen are important.

5.2 Physical considerations

5.2.1 Definition of maser action

A spectral line is said to exhibit maser action if the radiation is amplified by stimulated emissions as it moves through a medium. A necessary condition for this to occur is that the physical conditions are such that the relative population of the levels participating in the transition satisfy

$$\frac{N_n}{g_n} > \frac{N_{n'}}{g_{n'}} \tag{5.1}$$

for $n > n'$ and it is said that there is a population inversion between the levels. In this case, the number of stimulated emissions will exceed the number of absorptions and the line emission coefficient defined in equation (2.38) will become negative.

HRLs form together with the continuum radiation due to the free electrons in the source nebula. Therefore, a negative line absorption coefficient $\kappa_{n'n}$ is a necessary, but insufficient, condition for maser action. For a HRL maser to occur, the net absorption coefficient κ_ν, and therefore the net optical depth, must be negative so that for a homogenous nebula

$$\tau_\nu = (\kappa_{n'n} + \kappa_\mathrm{c})\, L < 0\,. \tag{5.2}$$

The quantity $|\tau_\nu|$ of a maser is called the maser gain, and a high gain maser will have $|\tau_\nu| > 1$. In this case, maser action will significantly affect the line intensities, as will be shown in section 6.1.2.

HRLs can be enhanced beyond their LTE intensities by stimulated emissions in two ways, even if the condition in equation (5.2) for maser action is not met. Firstly, Goldberg (1966) refers to the condition when $\kappa_{n'n} < 0$, but $\kappa_\nu > 0$ as the partial maser effect. Secondly, Strelnitski et al. (1996a) discuss the situation where the upper level of a line is overpopulated with respect to the LTE populations, but they are not strictly inverted so that condition (5.1) applies. In this case, the

line absorption coefficient is positive which Strelnitski et al. (1996a) referred to as being "overheated".

The amplification factor $\beta_{nn'}$ for a recombination nebula is shown in Fig. 4.6 for a range of conditions. The $\beta_{nn'}$ is an indication of the level of inversion between two levels. If $0 < \beta_{nn'} < 1$, the line will be overheated, and $\beta_{nn'} < 0$ indicates a population inversion as defined by equation 5.1. From the figure it is clear that almost all HRLs, except for the highest n-levels that will be thermalised, in a recombination nebula are either inverted or overheated. Almost all of the hydrogen atoms in a photoionised nebula are ionised, resulting in a very large reservoir of free electrons. This leads to large recombination rates (radiative and three-body) that favour the high n-levels creating a "pump" of electrons to the highly excited states. The spontaneous emission rates increase significantly with decreasing n, acting as a "sink" that depopulates the lower levels faster than they get populated through cascade from the higher levels. This means that the population inversions that occur in HRL masers are a natural consequence of the ionisation-recombination cycle, and no additional pumping scheme has to be invoked.

5.2.2 Angular momentum changing collisions

Strelnitski et al. (1996a) present some of the theoretical aspects of high gain HRL masers. They specifically focus on the optimum electron density for each maser line, i.e. the density at which the magnitude of the negative absorption coefficient $|\kappa_\nu|$ is maximized. In their calculations, they use departure coefficients derived from an n-model. They argue that the densities where maser lines are formed are high enough ($N_\mathrm{e} > 10^7\,\mathrm{cm}^{-3}$) that the angular momentum structure of the atoms can be ignored because the inelastic collisions will set up Boltzmann distributions among the l-levels. This sentiment has been echoed by Hengel & Kegel (2000).

It is true that the l-states for a particular n-level for $T_\mathrm{e} = 10^4\,\mathrm{K}$ and $N_\mathrm{e} = 10^8\,\mathrm{cm}^{-3}$ essentially have Boltzmann distributions for $n \geq 15$. However, in this case the nl-model still produces different results to the n-model due to the inclusion of elastic collisions. Fig. 5.1 shows the departure coefficients b_n and amplification factors for

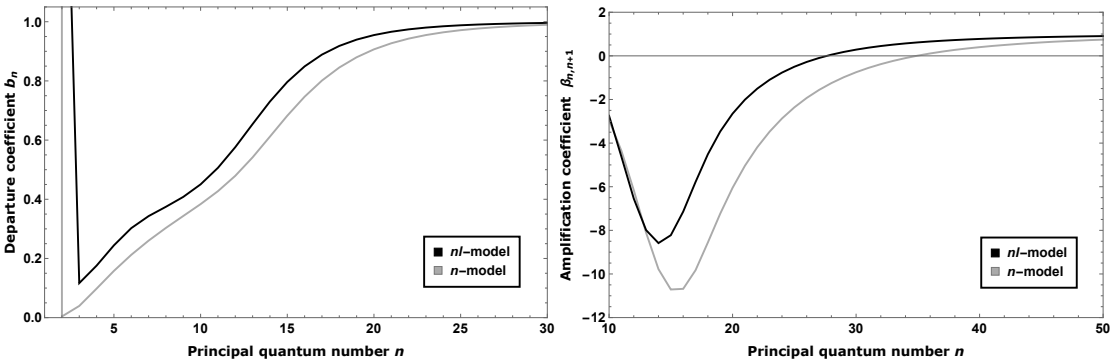

Figure 5.1 – The departure coefficients b_n and amplification factors for Hnα transitions $\beta_{n,n+1}$ produced by a C^3 model with $T_e = 10^4\,K$ and $N_e = 10^8\,cm^{-3}$ under the Case A assumption. The figures compare the results as produced by an n- and nl-model.

Hnα transitions $\beta_{n,n+1}$ from a C^3 model with $T_e = 10^4\,K$ and $N_e = 10^8\,cm^{-3}$ for Case A. The b_n's for the nl-model are calculated using equation 3.4. The elastic collisions set up Boltzmann distributions in the angular momentum states, but they also have the effect of moving the entire population of the n-level closer to LTE (b_n closer to 1) and reducing the inversions between levels (reducing $|\beta_{n,n+1}|$). I therefore used an nl-model to describe HRL masers, as the elastic collisions still have an effect on the overall level populations, even though most of the l-levels are statistically populated. The effect of accounting for the l-structure of the atoms is explored in section 6.1.3.

5.2.3 Free-free emission

In the case of a homogeneous pure hydrogen gas the intensity of the free-free emission generated by the electrons within a plasma is proportional to N_e^2. It is shown in section 4.3.3 that the effects of the free-free emission on level populations become increasingly important as the electron density increases. Therefore, it is important to include the free-free emission in model calculations of HRL masers that necessarily occur at high densities.

Strelnitski et al. (1996a) used departure coefficients from an n-model without free-free radiation included to draw their conclusions regarding conditions in which

hydrogen masers will form. The masers with the highest gain are calculated by considering the magnitude of the net absorption coefficients under various conditions. Their results have been found to be reasonably consistent with observations (Thum et al., 1998; Strelnitski et al., 1996b)

In contrast, the preceding discussion indicates that the angular momentum changing collisions and the free-free emissions should not be neglected at these densities. Both effects change the energy levels for which masing is possible by 5 to 10 levels, but at $N_e > 10^6\,cm^{-3}$ the two effects counteract one another when only considering $|\kappa_\nu|$. The inclusion of the angular momentum changing collisions narrows the range of possible n-levels from which H$n\alpha$ masers are possible whereas including the free-free emission widens the range. Neither effect changes the maximum value of $|\kappa_\nu|$ significantly, only the values of n where $\kappa_\nu < 0$ are altered. The partial cancellation of the two effects leads to the results of Strelnitski et al. (1996a) being consistent with a more sophisticated analysis.

5.3 The escape probability approach

5.3.1 Basic theory

A popular simplifying assumption when doing recombination line calculations is to assume that the emitting cloud is either completely opaque or completely transparent to particular lines. For example, the widely used Case B of Baker & Menzel (1938) assumes that all Lyman transitions are optically thick, whereas all others are optically thin. This assumption is very easy to incorporate into calculations and has been found to work well for nebular conditions where densities are low (Osterbrock, 1962).

When solving a C^3-type model, such as described in Chapter 3, it is standard to use the Case A/B assumption. In the case where line radiation is assumed to be optically thin ($\tau_\nu \ll 1$), diffuse radiation is assumed to escape the cloud without interacting with the particles. In the other extreme where the cloud is completely

optically thick to all line radiation ($\tau_\nu \gg 1$), all the level populations will follow Boltzmann distributions and the mean intensity $J_\nu = S_\nu$.

The EPA addresses the situation between these two extremes, such that a portion of the radiation is trapped in the cloud while some of it is allowed to escape. If the fraction of photons with frequency ν that escape the cloud is labeled β_ν (not to be confused with the amplification factor $\beta_{nn'}$), then $(1 - \beta_\nu)$ of the photons will be reabsorbed by the medium. With the fraction $(1 - \beta_\nu)$ of emitted photons trapped in the medium, the mean intensity can be approximated by (ignoring the continuum radiation fields for the moment)

$$J_\nu = (1 - \beta_\nu)\, S_\nu \,. \tag{5.3}$$

For an optically thin nebula, all photons escape the cloud so that $\beta_\nu = 1$. For maser transitions, which have inverted level populations, $\beta_\nu > 1$. Strictly speaking, β_ν depends on the full solution of the ERT, and cannot be calculated locally. However, if an approximation can be derived that depends only on the geometry and local properties of the cloud, and is independent of intensity, then the original problem is greatly simplified.

The EPA has been used extensively to model molecular masers. A popular form of the escape probability is the large velocity gradient (LVG) approximation (see for example Sobolev et al. (1997); Cragg et al. (2002); Langer & Watson (1984); Humphreys et al. (2001)). For a spherically symmetric, homogeneous cloud in which the expansion velocity is proportional to the radial distance from the centre, the escape probability becomes

$$\beta_\nu = \frac{1 - \exp\left(-\tau_\nu\right)}{\tau_\nu} \,. \tag{5.4}$$

Another feasible escape probability for masers is

$$\beta_\nu = \mathrm{e}^{-\tau_\nu} \tag{5.5}$$

as used, for example, by Kegel (1979); Koeppen & Kegel (1980); Chandra et al.

(1984); Röllig et al. (1999). The authors argue that this form of β_ν does not make any additional assumptions regarding the geometry or the changes in transfer effects throughout the line profile, and therefore is more appropriate to use if these details are not known. In this work equation (5.5) is used, because my aim is to derive general trends for which this form is more widely applicable. This results in the total mean intensity calculated by the model reducing to the sum of equations (2.45) and (2.46).

It should be noted that the results obtained from using equation (5.4) are very similar to those produced when using equation (5.5). When using the LVG approximation, path lengths of about a factor of two larger are required compared to the simpler equation (5.5) to obtain similar intensities for the masing lines.

5.3.2 Strengths and limitations

EPA methods are frequently applied to astronomical problems when the interest lies in overall line intensities emitted from a cloud rather than the exact details of line formation within the cloud. It is computationally easy to implement, and produces results that are in good agreement with much more sophisticated and calculationally complex methods (Elitzur, 1992). Notable radiative transfer codes such as Cloudy (Ferland et al., 2013), XSTAR (Kallman & Bautista, 2001) and RADEX (van der Tak et al., 2007) all make use of the EPA in various ways. However, the method is approximate and therefore its shortcomings should be taken into consideration when it is used.

EPA methods give an overall approximation of the global properties of a source. The level populations calculated in this formalism are independent of location in the source, and yield the mean level populations that are consistent with the overall emission. Importantly, the resulting level populations are consistent with saturation effects. Saturation occurs when the population difference between two levels of a maser transition is appreciably affected by the maser radiation. Therefore, the overall manner in which the maser emission affects the level populations is accounted for.

Uniform physical conditions throughout the source are a built-in assumption in this scheme, specifically a constant source function. However, the mean intensity J_ν is position-dependent through the optical depth. Because the source function also depends indirectly on J_ν, this is inherently contradictory. Elitzur (1992) argues that masers are particularly suitable to be treated in the EPA, due to the fact that maser source functions are essentially constant.

Elitzur (1990) emphasizes the importance of the effects of beaming when modelling masers. However, this is not a simple issue, as discussed in Lockett & Elitzur (1992), and the EPA can only account for this in a very approximate way. Because no particular geometry is assumed, and the model cloud is assumed to be homogeneous in this work, beaming effects are neglected.

Another limitation of the EPA is that it does not produce details about line shapes, only line integrated quantities (Asensio Ramos & Elitzur, 2018). The line profile of maser emission will change depending on the level of saturation (Elitzur, 1994). The details of this are lost in the EPA approach.

More accurate models for radiative transfer for multi-level atoms do exist. The gold standard is the accelerated Λ-iteration (ALI) method (Rybicki & Hummer, 1991) that does a much more detailed treatment of radiative transfer, but is also very computationally expensive. More recently, the coupled escape probability (CEP) method has been developed (Elitzur & Asensio Ramos, 2006; Asensio Ramos & Elitzur, 2018). The CEP method rivals the ALI methods in accuracy, but is much simpler to implement and faster to compute. However, neither accounts for saturation or beaming effects, and the CEP method defers to the more rudimentary EPA if saturation effects are important (Asensio Ramos & Elitzur, 2018). Gray et al. (2018) and Gray et al. (2019) present a three-dimensional model based on CEP that accurately accounts for beaming and saturation effects, but currently only under a two-level approximation.

All EPA formalisms are derived from plausibility arguments and not from first principles. This means that they provide no internal error estimate, and their accuracy can only be determined when their results are compared to those of full radiative transfer treatments like the ALI. Dumont et al. (2003) compared EPA

and ALI results with specific focus on AGN and X-ray binaries, and found that the EPA overestimates line intensities. Nesterenok (2016) also compared results from one-dimensional EPA and ALI models for methanol masers, and found that the EPA is accurate provided the cloud dimensions are large enough. Neither of these results are directly transferable to the EPA model presented here for hydrogen, but the limitations of this method should be kept in mind.

5.4 The model

5.4.1 Overview

The EPA model used here is similar to that of Hengel & Kegel (2000) with some important improvements. Most importantly, it includes the effects of the elastic collisions, so the calculations are done with a full nl-model. Also, the effects of free-free radiation on the level populations have been incorporated. Nevertheless, I use the same form of the escape probability and general calculational approach as Hengel & Kegel (2000).

My atomic model is based on the C^3 nl-model described in Chapter 3 that is adapted to incorporate radiative transfer using the EPA as described in section 5.3.1. All atomic rates are as described in Chapter 2. The iterative solver, as opposed to the direct solver, was used to obtain the b_{nl} values. This streamlined the calculations which had to be repeated many times for increasing path lengths. Because the n-model results became unreliable for large path lengths, the value of n up to which the nl-model is calculated is increased considerably from what is used in Chapter 3. This is discussed further in section 6.1.1.

A box profile with the same amplitude as the Doppler profile is assumed for all lines so that

$$\phi_\nu = \begin{cases} \frac{1}{\sqrt{\pi}\nu_\mathrm{D}} & \text{for } |\nu - \nu_0| < \frac{\sqrt{\pi}\nu_\mathrm{D}}{2} \\ 0 & \text{otherwise} \end{cases} \tag{5.6}$$

where

$$\nu_{\mathrm{D}} = \frac{\nu_0}{c}\sqrt{\frac{2kT_{\mathrm{e}}}{m_{\mathrm{e}}}}\,. \tag{5.7}$$

The SBE as described in Chapter 3 are not a closed system. Details regarding the ionising radiation are not specified, and therefore the population of the ground state cannot be calculated. In addition to the SBE, the degree of ionisation $\zeta = N_0/N_{\mathrm{e}}$, where N_0 is the number density of neutral hydrogen, is fixed to $\zeta = 10^{-4}$. The total number density of neutral hydrogen is equal to the number densities of atoms with electrons in all bound states, so that

$$b_1 = \frac{N_{\mathrm{e}}}{N_1^*}\left(\zeta - \sum_{n=2}^{n_{\max}} \frac{b_n N_n^*}{N_{\mathrm{e}}}\right)\,. \tag{5.8}$$

5.4.2 Calculational procedure

First, the SBE are solved in the optically thin case ($\beta_\nu = 1$) for all lines to yield departure coefficients that are equivalent to the ones calculated by the C^3 model for Case A. From the calculated values of b_{nl}, the net absorption coefficients, emission coefficients and source functions are calculated for each line using equations (2.37), (2.39) and (2.42).

The path length L is then increased, and the optical depths and escape probabilities are calculated from equations (2.36) and (5.5), respectively. Because the escape probabilities become unstable near $\tau_\nu = 0$, a Taylor expansion is used for small values of τ_ν. The resulting mean intensities are calculated for each line using equation (5.3). The SBE are solved again with these values of J_ν incorporated into the rates of the stimulated processes. The process is repeated for increasing values of L.

Because the atomic rates on which the departure coefficients depend have inherent inaccuracies, the b_{nl} values cannot be calculated to an arbitrary precision. The line absorption coefficients depend on the ratios of departure coefficients, and therefore are highly sensitive to numerical errors in the b_{nl}'s. At high column densities, the

line absorption coefficients become unstable and exhibit oscillating behaviour. This occurs abruptly as iterations over L are performed.

Small inaccuracies in the b_{nl}'s are amplified by the strong dependence of both β_ν and J_ν on κ_{mn} as the iterative process progresses. This is especially true in the region where $|\kappa_{mn}| > \kappa_{\rm c}$ which is where masing can occur. The procedure is stable up until the point where the $\kappa_{n,n+1}$ start to develop minor oscillating behaviour; these perturbations are exaggerated to unphysical results within a few iterations. The point in the procedure where the results become unstable has been extended by applying a moving average filter to both the $\kappa_{n+1,n}$ and J_ν for H$n\alpha$ transitions at large values of L. This is a common method used for smoothing data affected by noise. In this case, the mean of blocks of 3 points are calculated in the region where $\kappa_{n,n+1} < 0$. For a data set x_i, the smoothed data is given by

$$\bar{x}_i = \frac{1}{3} \sum_{k=i-1}^{i+1} x_k \,. \tag{5.9}$$

The breakdown of the model at high column densities is not that limiting in practice when compared to available observations. The intensities of H$n\alpha$ transitions from MWC 349A are well within the limits of this model (see section 6.1.4).

Chapter 6

HRL maser model results

6.1 Results and discussion

6.1.1 Conditions for hydrogen masers

The pumping mechanism for hydrogen masers is the ionisation-recombination cycle, so it is important that the gas is ionised. A typical ionised nebula is assumed to have a temperature $T_\mathrm{e} \sim 10^4$, but mechanisms such as bright forbidden line emission due to high metallicity can cool the gas while keeping the hydrogen mostly ionised. If the electron temperature is too high, the interactions between the free and bound electrons become much more effective than any other atomic process and the populations of the bound electrons thermalise. A temperature range of $3\,000\,\mathrm{K} \leq T_\mathrm{e} \leq 15\,000\,\mathrm{K}$ is considered here.

Spectral lines will exhibit high-gain maser action if the conditions are such that stimulated emissions become the dominant atomic process and $\tau_\nu < -1$. This requires a large column density along the line of sight, which can be achieved either with high number densities of hydrogen atoms or long path lengths. The model results show that a path length of $L \sim 10^{16}\,\mathrm{cm}$ is required to produce maser action at a density of $10^6\,\mathrm{cm}^{-3}$. Each order of magnitude decrease in N_e results in about an order of magnitude increase in L to produce a maser. Maser action

requires velocity coherence along the amplification path, which puts an upper limit on L. Therefore, electron densities $N_e \geq 10^7\,\mathrm{cm}^{-3}$ are considered here.

For densities higher than $N_e \sim 10^{10}\,\mathrm{cm}^{-3}$ the net absorption coefficient is negative for $n \leq 10$, so that theoretically masing is possible for these lines. However, the population of the ground level is set artificially to a fixed level of ionisation in this model, so the results for the lowest n-levels are probably not very accurate and densities above this threshold are not considered. It is also unlikely that a gas of this density will be sufficiently ionised for recombination lines to be produced.

6.1.2 General trends

Fig. 6.1 shows how the line centre intensities, calculated using the first term of equation (2.45), change as the path length is increased in my model for various H$n\alpha$ transitions. For small path lengths, the intensities of all lines increase linearly with path length, as is expected for optically thin lines. The behaviour of the line intensities change when $|\tau_\nu| > 1$ in one of two ways, depending on whether τ_ν is positive or negative.

For the conditions shown in Fig. 6.1, the lines with $n \geq 40$ have positive optical depths which increase as n increases throughout the iterations over path length. The level populations for these lines are not strictly inverted, but are "overheated" as discussed in section 5.2.1. These line intensities increase linearly with path length until the cloud becomes larger than their characteristic path length (for which $\tau_\nu = 1$). Because the lines cannot be observed from deeper in the cloud than their characteristic path length, once they are optically thick, their intensities remain constant even if the size of the cloud is increased. Because τ_ν for the H$n\alpha$ lines increases with n, the lower frequency (higher n) lines become optically thick before the lower n lines as L increases.

The optical depths of the H20α and H25α lines are negative, and their intensities start to increase exponentially with distance once $\tau_\nu < -1$ for their respective optical depths, and maser action sets in. The case of H30α is interesting, because

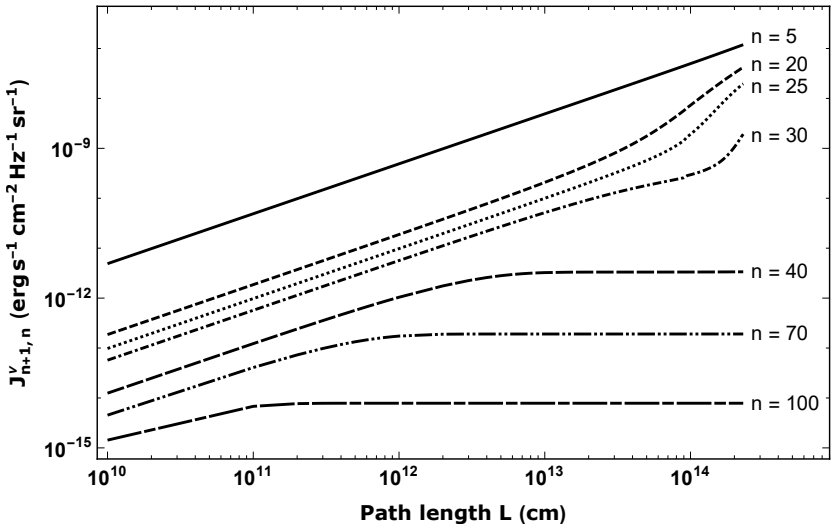

Figure 6.1 – The change of the intensities at line centre for various H$n\alpha$ transitions with path length for a gas at $T_\mathrm{e} = 10^4\,\mathrm{K}$ and $N_\mathrm{e} = 10^8\,\mathrm{cm}^{-3}$.

its optical depth is positive for small path lengths, but it is "attracted" into the masing range as masing in adjacent lines become effective. This phenomenon is discussed in more detail in section 6.1.3. I do not expect the exponential growth to continue indefinitely, but because the model becomes unstable as the path length increases I cannot investigate this region of phase space. The optical depth of the H5α line is also negative, but $\tau_\nu > -1$ for path lengths $L < 10^{15}\,\mathrm{cm}$ which is where this model is terminated.

Fig. 6.2 shows the line intensities for H$n\alpha$ lines in a gas with $T_\mathrm{e} = 10^4\,\mathrm{K}$ and $N_\mathrm{e} = 10^8\,\mathrm{cm}^{-3}$ as a function of n for different path lengths. The intensities increase for all n from the optically thin values as L is increased, as is also illustrated in Fig. 6.1. As L increases, the lines get optically thick from high values of n, and then do not increase further. If the path length becomes large enough that $\tau_\nu < -1$ for some lines, a bump starts to appear, indicating maser action in those lines. As the path length is increased further, the intensities of the masing lines increase significantly with L, making the bump more pronounced.

The observable intensities, as calculated using equation (2.44) are shown in Fig. 6.3 for comparison with Fig. 6.2. The quantity $\bar{J}^{\nu}_{n+1,n}$ does not behave as one would expect for the intensity of a spectral line. For example, the brightness of $\bar{J}^{\nu}_{61,60}$ is

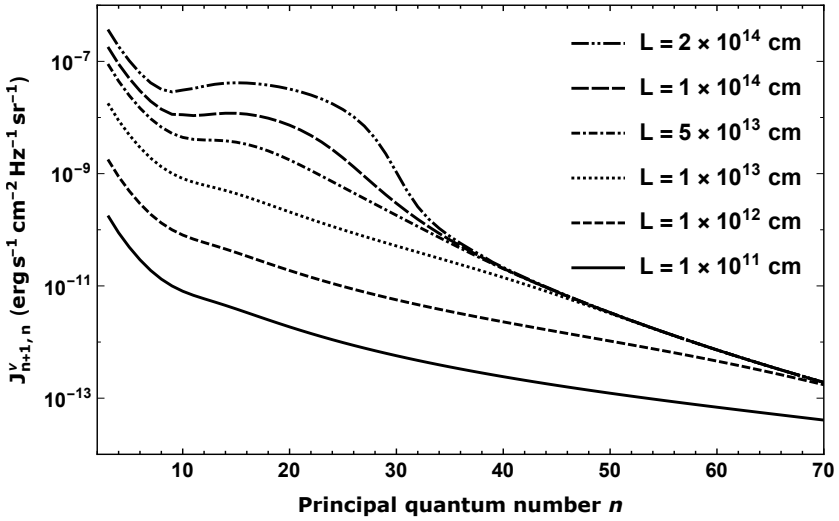

Figure 6.2 – Intensities at line centre of H$n\alpha$ transitions with respect to principal quantum number for a gas with $T_\mathrm{e} = 10^4\,\mathrm{K}$ and $N_\mathrm{e} = 10^8\,\mathrm{cm}^{-3}$ for different path lengths.

decreased if the path length along the line of sight is increased from $L = 10^{12}$ cm to $L = 10^{14}$ cm.

The discrepancy between $\bar{J}^\nu_{nn'}$ and $J^\nu_{nn'}$ is due to the photons within the width of the line all experiencing an optical depth τ_ν, regardless of whether they are emitted by atomic transitions or as part of the continuum by the free electrons. Equation (2.44) assumes that continuum photons are isolated from the atoms in the gas and do not interact with them.

If maser action is present in the line then $\bar{J}^\nu_{n+1,n} > J^\nu_{n+1,n}$. This occurs because the continuum photons will also be enhanced by stimulated emission thereby contributing to the observable intensity at the line centre. This scenario is illustrated in Fig. 6.4(a). On the other hand, in a non-masing line with a large positive optical depth ($\tau_\nu > 1$), $\bar{J}^\nu_{n+1,n} < J^\nu_{n+1,n}$ so that the observed line intensity will underestimate the contribution of the line photons to the total emission observed in the line, as shown in Fig. 6.4(b). This discrepancy increases as the magnitude of the optical depth increases, or, for the case illustrated in Figs. 6.2 and 6.3, as the path length is increased.

Fig. 6.5 illustrates the effect of the electron density on the emitted spectrum of H$n\alpha$

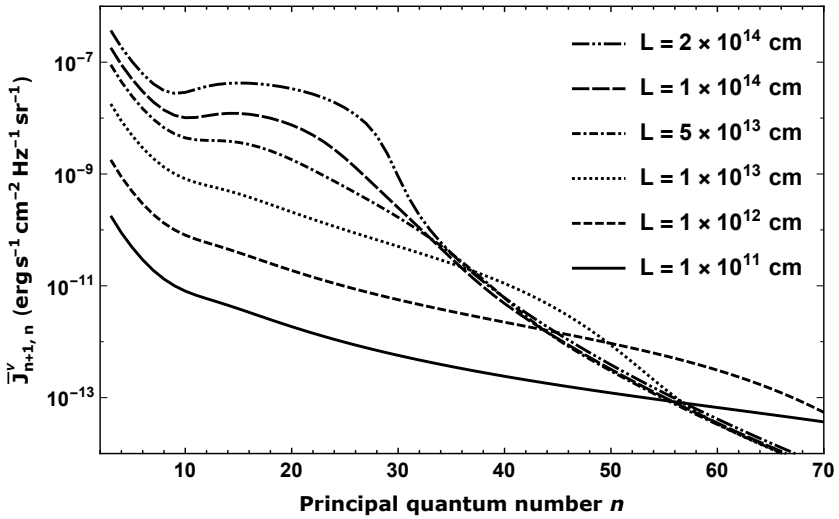

Figure 6.3 – Observable intensities at line centre of H$n\alpha$ transitions with respect to principal quantum number for a gas with $T_\mathrm{e} = 10^4\,\mathrm{K}$ and $N_\mathrm{e} = 10^8\,\mathrm{cm}^{-3}$ for different path lengths.

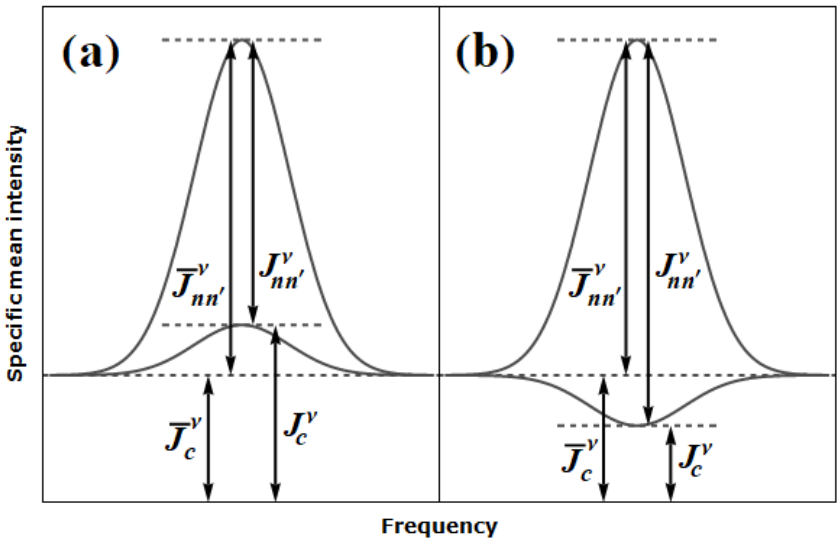

Figure 6.4 – The effects of optical depths on the line and continuum radiation within a spectral line. The left panel shows the situation for $\tau_\nu < -1$ and the right panel shows the situation for $\tau_\nu > 1$

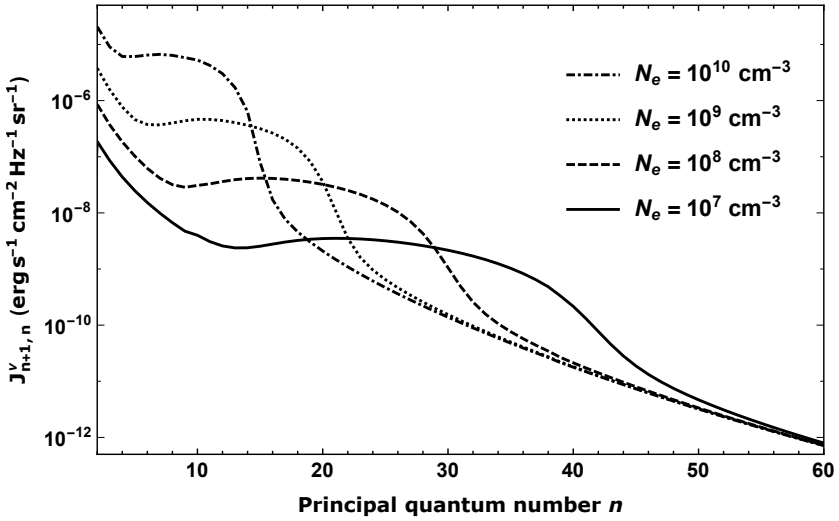

Figure 6.5 – Emitted spectrum of H$n\alpha$ transitions for masing region at electron temperature $T_{\rm e} = 10^4$ K for a range of electron densities.

lines. The kinetic temperature is the same for all of the models shown ($T_{\rm e} = 10^4$ K) and the path length is chosen to show a pronounced bump for each case. The H$n\alpha$ lines that exhibit masing are mostly determined by the electron density, with masing occurring at lower n-levels for higher densities. The behaviour of the the H$n\alpha$ lines in the optically thick regime (high n) is independent of density.

The effects of temperature on the emitted spectrum of a hydrogen maser region are much less pronounced than that of electron density. The values of n where maser action occurs increase slightly towards higher n-levels as the temperature increases.

6.1.3 Comparison with optically thin and n-model results

Departure coefficients calculated assuming optically thin conditions (C^3 models) are often used as a first approximation when doing HRL maser calculations, see for example Strelnitski et al. (1996a) and Báez-Rubio et al. (2013). It has also been argued that, due to the high densities at which HRL masers occur, it is reasonable to neglect the l-structure of the atoms and use the results of an n-model (Strelnitski et al., 1996a; Hengel & Kegel, 2000).

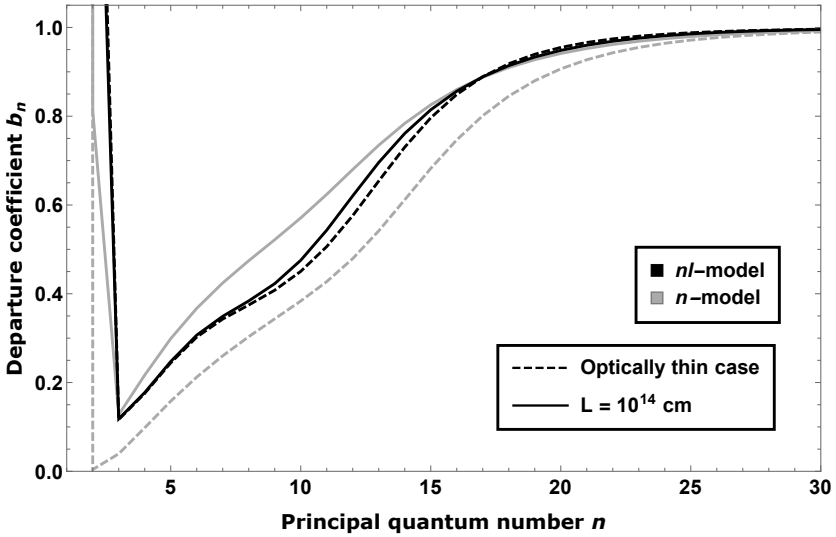

Figure 6.6 – Departure coefficients b_n for the n-levels for a gas with $T_\mathrm{e} = 10^4\,\mathrm{K}$ and $N_\mathrm{e} = 10^8\,\mathrm{cm}^{-3}$ as calculated by the n- and nl-models under optically thin conditions (same as shown in Fig. 5.1) and for an EPA model with $L = 10^{14}\,\mathrm{cm}^{-3}$.

The effects on the departure coefficients b_n when using an n- vs an nl-model are shown in Fig. 6.6. The dashed lines show the departure coefficients for the optically thin case, and are the same as depicted in Fig. 5.1. The solid lines show how the level populations change in the two types of models when the EPA is applied.

Fig. 6.7 shows the line absorption coefficients at line centre of H$n\alpha$ as calculated using the level populations from models with different assumptions. Using the optically thin n-model results overestimates the maser gain by a factor of a few. Both the n-models (C^3 and EPA) overestimate the range of H$n\alpha$ transitions that can exhibit masing towards higher n-levels for a given set of conditions. The two nl-model results are similar, so that deciding which to use will depends on the accuracy required for a specific application. The EPA nl-model predictions are more accurate than the C^3 nl-model results in two ways, namely the n-level where the most maser gain will be seen and the range of lines over which maser action can occur.

Fig. 6.8 shows the predicted line intensities if level populations from a C^3 nl-model are used as opposed to those from the EPA nl-model that are illustrated in

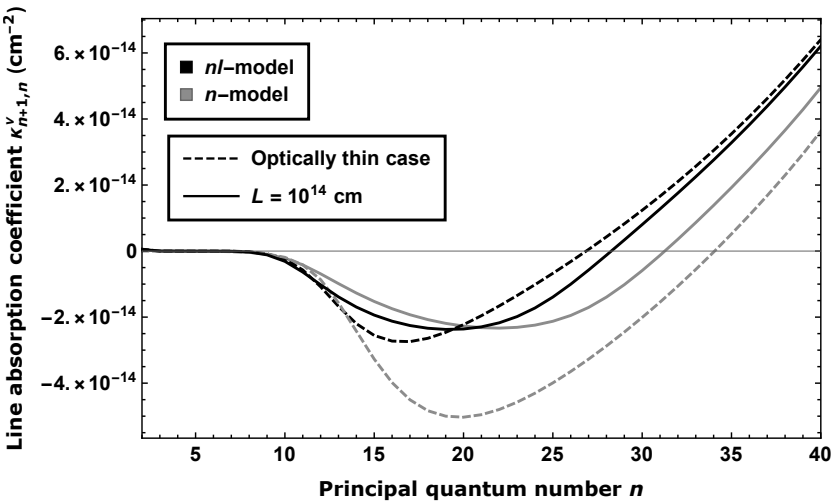

Figure 6.7 – Absorption coefficients at line centre for H$n\alpha$ transition lines as calculated by different model assumptions as indicated in the legend. The electron temperature was set to $T_{\rm e} = 10^4\,{\rm K}$ and the electron density to $N_{\rm e} = 10^8\,{\rm cm}^{-3}$.

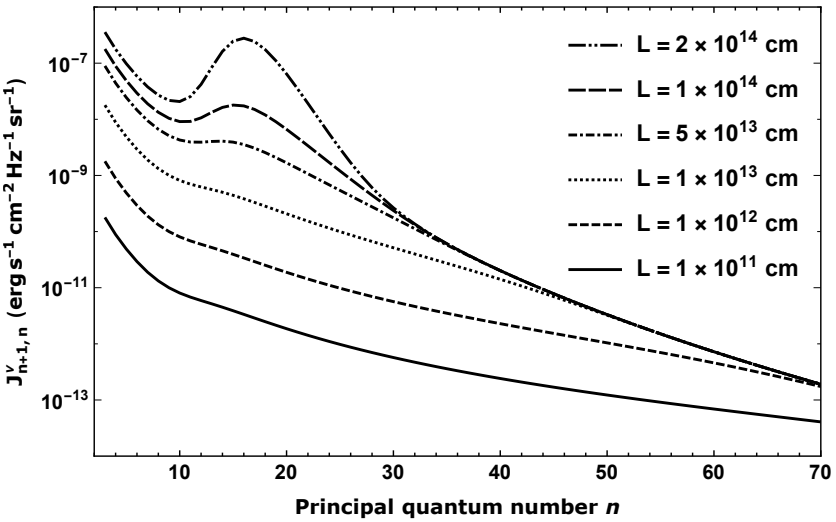

Figure 6.8 – Similar to Fig. 6.2, but using b_{nl} values calculated in the optically thin approximation for all path lengths.

Fig. 6.2. In the C^3 case, the maximum maser gain is shifted to a lower n-level and the bump feature is much sharper due to the level populations not being changed by the diffuse radiation. Using the C^3 n-model results show a similar trend, but with the bump feature much exaggerated, as expected from the large magnitude of the line absorption coefficient shown in Fig. 6.7.

Strelnitski et al. (1996a) discuss the possibility of saturation in higher frequency lines "attracting" lower frequency lines to exhibit masing. If, for example, saturation in one of the masing lines, say $2 \rightarrow 1$, will cause a decrease in the upper level of the transition, level 2. This will increase the inversion between levels 3 and 2, and therefore the $3 \rightarrow 2$ line will increase in intensity. If this process is effective enough, masing will start in the $3 \rightarrow 2$ transition, and the mechanism can diffuse out to even higher levels.

This behaviour is seen in the EPA model as illustrated in Fig. 6.9, which shows how the total optical depths at certain H$n\alpha$ line frequencies changes as L is increased. The optical depths at the H27α to H30α transition frequencies are positive for small values of L, and become negative and start to exhibit masing behaviour at some larger value of L. This occurs when the H$n\alpha$ transitions for lower n-levels' degree of saturation have increased enough to increase the inversion of higher transitions, expanding the range of lines where maser action is possible.

6.1.4 Comparison with observations

I compare results from the model with observations obtained by Thum et al. (1995) and Thum et al. (1998) for MWC 349A. This is the best studied hydrogen maser region at present with intensity data available over a large range of frequencies. Aleman et al. (2018) more recently published observations of the nebula Mz 3 in which hydrogen masing is also observed. The line intensity ratios of Aleman et al. (2018) are very similar to those of Thum et al. (1998), but the observations cover a much smaller frequency range than for MWC 349A. The limited observations do not show the complete bump structure in the H$n\alpha$ spectrum, so the model presented here cannot be used to constrain the physical parameters adequately.

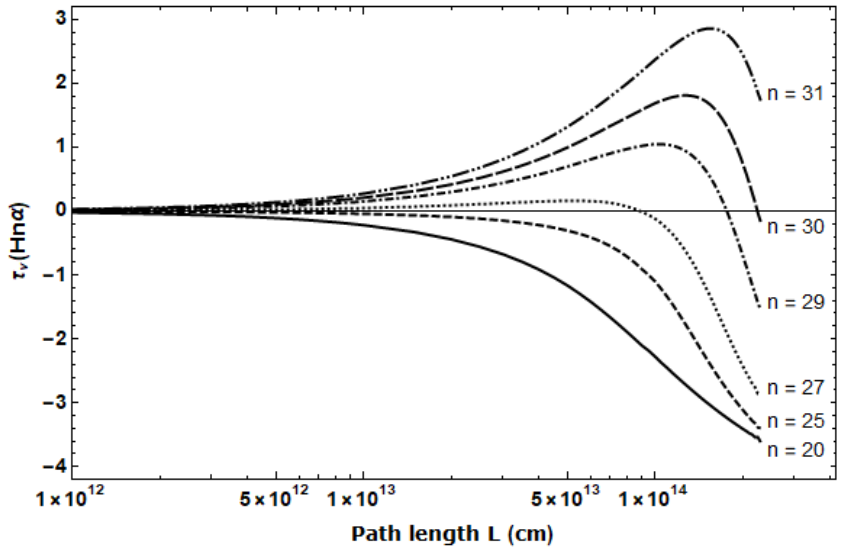

Figure 6.9 – The change in optical depths with increasing path length for selected H$n\alpha$ transitions under conditions of $T_\mathrm{e} = 10^4\,\mathrm{K}$ and $N_\mathrm{e} = 10^8\,\mathrm{cm}^{-3}$.

The three sets of data that were used to find a reasonable model are the H$n\alpha$ fluxes from Thum et al. (1998), the β/α ratios for which the lines are close in n from the same paper, and the β/α ratios for which the lines are close in frequency from Thum et al. (1995). An H$n\beta$ line represents the transition $n+2 \rightarrow n$. The best fit results from the EPA model that gave a reasonable fit considering all three sets of data occur for $T_\mathrm{e} = 11\,000\,\mathrm{K}$, $N_\mathrm{e} = 7 \times 10^7\,\mathrm{cm}^{-3}$ and $L = 2.7 \times 10^{14}\,\mathrm{cm}$. These parameters are similar to the values obtained by Báez-Rubio et al. (2013) for the disc of MWC 349A which is the putative source of the maser emission. It is possible to get a model that matches one of the sets of data better than the chosen model, but it would be very inaccurate for the others. The aim of this fit is not to determine exact properties of MWC 349A, but to show that the EPA model gives results consistent with current observations

Fig. 6.10 compares the data of Thum et al. (1998) and the chosen fit produced by the current model. The figure shows the observable integrated line intensities $\bar{J}_{n+1,n}$ obtained from equation (2.44) of H$n\alpha$ transitions relative to the H10α intensity. The model greatly underestimates the observable intensities for lines with $n > 40$. It is believed that observed α-lines with $n > 38$ originate in the outflow and not in the disc where the masers are formed (Planesas et al., 1992).

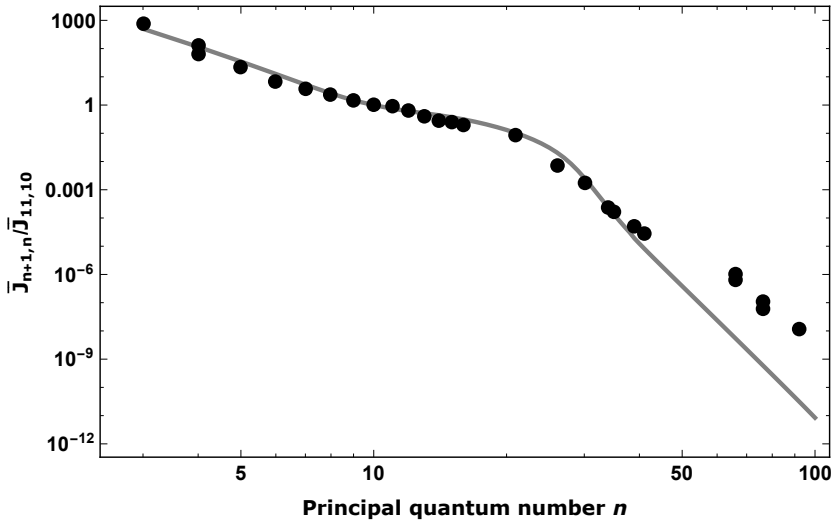

Figure 6.10 – Results from the model (solid line) compared to data from Thum et al. (1998) (circles) for integrated line intensities of H$n\alpha$ transitions relative to H10α. $T_\mathrm{e} = 11\,000\,\mathrm{K}$, $N_\mathrm{e} = 7 \times 10^7\,\mathrm{cm}^{-3}$ and $L = 2.7 \times 10^{14}\,\mathrm{cm}$.

Fig. 6.11 shows the ratios of the integrated observed H$n\beta$ and H$n\alpha$ lines with the same upper level (black circles) for the model (solid line) shown in Fig. 6.10. Agreement between the observations and model is good, except for the lowest n levels. Because the population of the ground level is set artificially to a fixed degree of ionisation, the results for the lowest n levels are not reliably determined by the model. The figure also shows the model predictions for the ratio for $n > 16$. The results for $n > 40$ will probably not be observed, since the measured lines from MWC 349A at those frequencies are not emitted from the disc. A list of H$n\alpha$, H$n\beta$ and H$n\gamma$ lines that occur within the frequency bands of ALMA is given in Table 6.1.

A comparison between my model results for $T_\mathrm{e} = 11\,000\,\mathrm{K}$, $N_\mathrm{e} = 7 \times 10^7\,\mathrm{cm}^{-3}$ and $L = 2.7 \times 10^{14}\,\mathrm{cm}$ and the observations of Thum et al. (1995) for β/α ratios that are close in frequency is presented in Table 6.2. Most ratios could be fitted within the given ranges of Thum et al. (1995). The worst outlier is the ratio $48\beta/40\alpha$, which is consistent with the model's inability to fit lines with $n > 40$.

Table 6.1 – List of H$n\alpha$, H$n\beta$ and H$n\gamma$ lines that occur in the ALMA frequency bands.

Upper level	Line	ν (10^{11} Hz)	ALMA band	Upper level	Line	ν (10^{11} Hz)	ALMA band
20	H19α	8.880	10	38	H35γ	4.071	8
22	H21α	6.624	9	38	H36β	2.600	6
25	H24α	4.475	8	39	H37β	2.400	6
26	H24β	8.444	10	40	H37γ	3.468	7
26	H25α	3.969	8	40	H38β	2.220	6
27	H26α	3.536	7	41	H38γ	3.210	7
28	H26β	6.700	9	41	H39β	2.058	5
28	H27α	3.164	7	42	H39γ	2.978	7
29	H28α	2.843	7	42	H40β	1.911	5
30	H27γ	8.570	10	43	H40γ	2.767	7
30	H29α	2.563	6	43	H41β	1.777	5
31	H29β	4.882	8	44	H41γ	2.576	6
31	H30α	2.319	6	44	H42β	1.656	5
32	H29γ	6.987	9	45	H42γ	2.402	6
32	H30β	4.424	8	45	H43β	1.546	4
32	H31α	2.105	5	46	H43γ	2.244	6
33	H30γ	6.341	9	46	H44β	1.445	4
33	H31β	4.022	8	47	H44γ	2.099	5
33	H32α	1.917	5	47	H45β	1.352	4
34	H32β	3.667	7	48	H45γ	1.966	5
34	H33α	1.750	5	48	H46β	1.268	4
35	H33β	3.352	7	49	H46γ	1.844	5
35	H34α	1.602	4	50	H47γ	1.733	5
35	H34α	1.602	5	51	H48γ	1.630	4
36	H33γ	4.823	8	51	H48γ	1.630	5
36	H34β	3.073	7	52	H49γ	1.535	4
36	H35α	1.470	4	53	H50γ	1.447	4
37	H34γ	4.425	8	54	H51γ	1.366	4
37	H35β	2.823	7	55	H52γ	1.290	4
37	H36α	1.353	4				

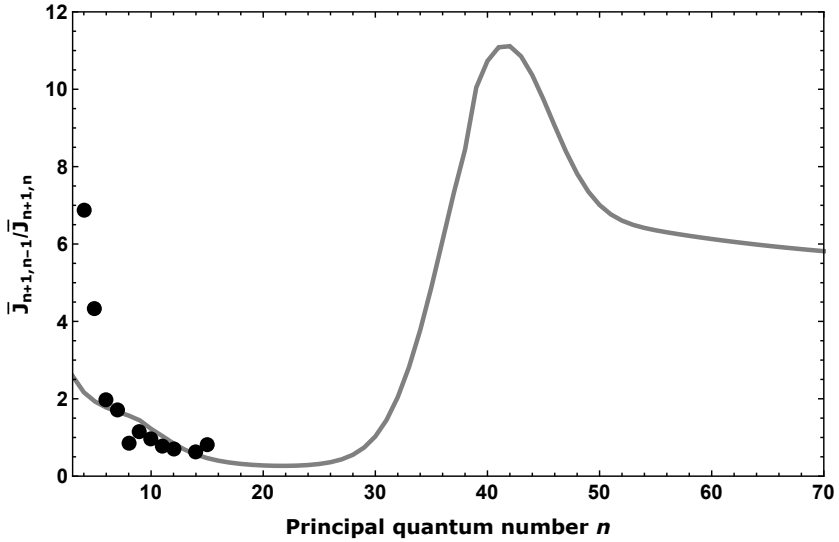

Figure 6.11 – The ratio of H$n\alpha$ and H$n\beta$ lines with the same upper level. Circles show observations from Thum et al. (1998), the solid line shows results from the same model as in Fig. 6.10.

Table 6.2 – Model results compared to observed ratios of H$n\beta$/H$n\alpha$ pairs that are close in frequency as published by Thum et al. (1995).

Lines	Model ratio (%)	Observed ratio (%)
$37\beta/30\alpha$	9.9	< 12
$33\beta/26\alpha$	4.2	< 10
$39\beta/31\alpha$	9.3	12 ± 3
$33\beta/26\alpha$	4.2	8.5 ± 1.5
$32\beta/26\alpha$	5.6	4.5 ± 1.5
$45\beta/36\alpha$	15	< 18
$38\beta/30\alpha$	7.1	6.6 ± 1.5
$48\beta/40\alpha$	31	14 ± 2

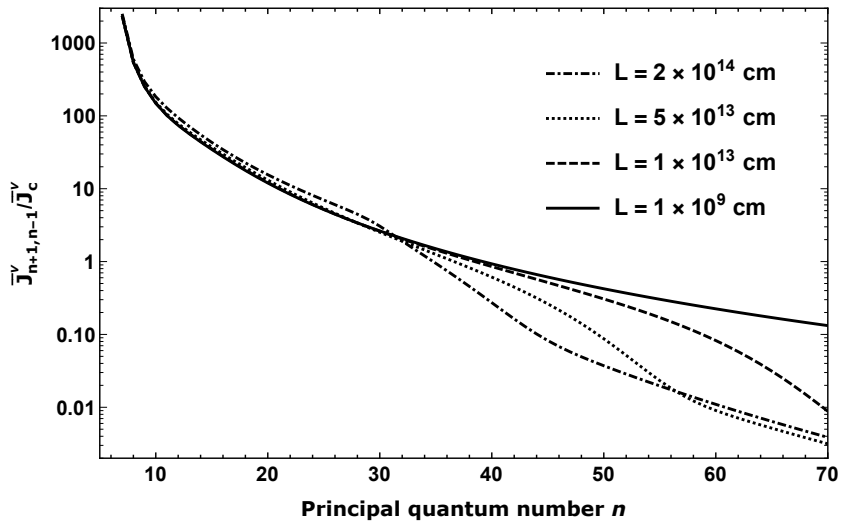

Figure 6.12 – The ratio of the observed line centre to continuum intensities of H$(n-1)\beta$ lines for a gas with $T_{\rm e} = 10^4\,{\rm K}$ and $N_{\rm e} = 10^8\,{\rm cm}^{-3}$ for various path lengths.

6.1.5 Ratios of α- and β-lines

Comparing the intensities of H$n\beta$ lines to those of H$n\alpha$ transitions can provide additional information regarding the physical conditions in the emitting region. Strelnitski et al. (1996b) concluded that it is preferable to consider β/α pairs that are close in n-value for masing regions, as opposed to pairs that are close in frequency. This section reviews some general theoretical trends that should be observable in masing regions.

Fig. 6.12 is a plot of the ratio of the line intensity $\bar{J}^{\nu}_{n+1,n-1}$ and continuum $J^{\nu}_{\rm c}$ vs n which gives an indication of the observability of H$(n-1)\beta$ transitions (i.e. $n+1 \rightarrow n-1$) for a masing gas. The solid line in the graph is an approximation of the optically thin case. As the path length is increased, the β-lines are slightly enhanced in the same n-region as the α-lines, but they are not technically masing. The observable line to continuum ratio decreases as the path length is increased for the higher n-transitions.

Because the α-transitions have a larger transition probability than the β-transitions, for a single emitting atom, the intensity of the α-lines will always be greater than

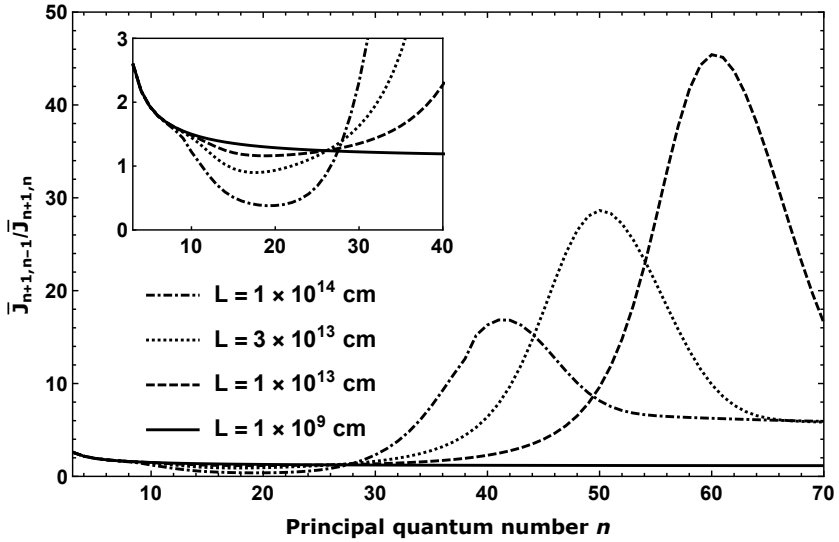

Figure 6.13 – The model ratios of β- and α-lines with the same upper level for a masing gas with $T_\mathrm{e} = 10^4\,\mathrm{K}$ and $N_\mathrm{e} = 10^8\,\mathrm{cm}^{-3}$ for various path lengths. The inset magnifies the behaviour at small n.

or equal to the intensity of the β-lines. However, when considering a cloud, the difference in optical depths of the two transitions plays an important role. The optical depths of the α-transitions are much larger than those of the β-transitions for the same upper level, so that the α-lines will always have a higher optical depth than their β counterparts in the region where masing is not present.

Fig. 6.13 shows the behaviour of the observable integrated intensities $\bar{J}_{n+1,n-1}/\bar{J}_{n+1,n}$ as a function of n for the case $T_\mathrm{e} = 10^4\,\mathrm{K}$ and $N_\mathrm{e} = 10^8\,\mathrm{cm}^{-3}$ for a range of values of L as produced by the EPA model. In the region where the H$n\alpha$ lines exhibit masing (inset in Fig. 6.13), the ratio is decreased as L increases, and the α-lines outshine the non-masing β-lines. At high values of n the situation is reversed, with the β-lines becoming more intense than the α-lines.

For example, for the $L = 10^{14}\,\mathrm{cm}$ case shown in Fig. 6.13 the line optical depths at line centre are $\tau_{41,40} = 6$ and $\tau_{41,39} = 0.8$. This means that the characteristic path length of a β-photon is larger than that of an α-photon by a factor of about 7.5, i.e. we are observing β-photons coming from 7.5 times deeper in the cloud than the α-photons. Therefore, the observed intensities of the β-lines are much brighter than those of the α-lines if one or both of the transitions become optically thick.

If both of the transitions are optically thick, the integrated intensity ratio of the two lines will tend to ~ 5, regardless of physical conditions.

The bump feature that emerges in Fig. 6.13 between the masing region and where both lines are optically thick is due to the interaction between the line and continuum opacities for the observable intensities. The maximum of the bump occurs at a point where $\tau_{\rm c} \approx 1.5$ for the β-lines.

Chapter 7

Conclusion

7.1 Summary

HRLs from astronomical gasses have been investigated by constructing computer models that focus on the atomic physics involved in the formation of these spectral lines. The effects of absoption and stimulated emission on line intensities have been investigated, both due to continuum fields in optically thin nebular gasses and in the more extreme case of HRL masers. Both of these models have produced new results that enhance our general understanding of the physics and the modelling of these objects.

Updated calculations of departure coefficients for hydrogen atoms under nebular conditions are presented. The elastic collision rates of Guzmán et al. (2016) have been used, which differ from values used in previous models. I have also included stimulated and absorption processes in my equations of statistical equilibrium. The model used to do the calculations is similar to that of SH95.

A stopping criterion has been derived and employed to determine when to terminate the iterative procedure, which ensures that the b_{nl} values have converged to a predefined accuracy. This requires that many more iterative steps are required before a solution is reached than have been used in previous works. In practice, I

found that it is more time efficient to use a direct solver rather than the iterative method to achieve an acceptable accuracy.

I investigated the effects of absorption and stimulated emission due to various components of the continuum field within a nebula on the population structure of hydrogen. Even though the stellar radiation field and emission from dust dominate the continuum spectrum at certain frequencies, the effects of both fields on the population structure are negligible. The free-free radiation field has the largest influence on the departure coefficients, increasing as the density increases. The CMBR typically has an effect of less than 1 per cent on the departure coefficients.

My results give departure coefficients that are consistently larger (closer to LTE) than those of SH95. The current results produce amplification factors $\beta_{n,n+1}$ that are smaller than in previous calculations, producing less extreme population inversions. The value of $n_{\rm c}$, the level at which populations become statistically distributed, has been determined empirically. The value, which depends on the electron density $N_{\rm e}$, is much larger than used in models by other authors.

HRL masers are a relatively new field in astronomy, with only a handful of observational examples and limited work done so far on their theoretical framework. The modelling of masers has some inherent complexities, since both the local level populations of the masing species and the non-local radiative transfer of the line photons have to be solved simultaneously in principle. Simplifying assumptions are often employed, for example the EPA used in this work. The EPA has limitations, but it is also a very useful tool to gain insight into overall emission from a cloud.

A model for hydrogen recombination masers using the EPA has been constructed to evaluate the general behaviour of hydrogen emission from clouds with conditions where masing is possible. The observable effects of line-of-sight path length, electron temperature and electron density on the intensities of H$n\alpha$ emission lines have been investigated and discussed. The model results for varying path length corresponds well to our current understanding of how masers grow with increasing path length. The electron density has the biggest effect on which transitions will exhibit masing. It has been emphasised that there is a difference between

the observable line intensity $\bar{J}^{\nu}_{nn'}$ and the contribution of line photons to the total intensity $J^{\nu}_{nn'}$ under optically thick conditions.

A fit of the model results was done to observations of the region MWC 349A where masing in hydrogen was first discovered. A good fit is obtained over the range of frequencies where maser action occurs with physical parameters in line with what other authors have obtained.

The behaviour of the ratios of H$n\alpha$ and H$n\beta$ lines that form from the same upper level have been examined. A fit was done to high frequency observations that are available, and model predictions for lower frequency transitions are shown.

7.2 Future work

The C^3 model will be updated to model helium and metal atoms and ions. Departure coefficients for these species where the stopping criterion that was derived in this work is used are currently not available. Considering that the implementation of said stopping criterion changed the departure coefficients of hydrogen significantly under certain conditions, the same might be true for other atoms and ions. The hydrogen model forms the basis of more complex models, so the current model can be built on to simulate other elements.

The maser model will be applied to observations from objects besides MWC 349A, to explore additional conditions that might affect maser emission from HRLs. For example, Murchikova et al. (2019) propose that the masing HRL region that they studied is permeated by intense continuum radiation emanating from Sgr A*. Including such a radiation field in the current model would be straightforward. However, they, like many other authors, only looked at the H30α line and my results suggest that observations of several masing lines might be necessary to use a model such as mine to constrain the physical conditions of the emitting medium.

Zhang et al. (2019) recently discovered possible masing in the helium line He30α toward a protostellar object. This would be the first recombination line maser in

helium detected and my current hydrogen model needs to be modified to examine conditions where helium masers could exist. Possible candidates for such masers are hydrogen deficient novae, such as V445 Pup (Ashok & Banerjee, 2003), but more theoretical work is needed to understand how they might form and where to look for them.

Observations are needed to test the results and predictions of the maser model presented in this work. Specifically, the ratios of the H$n\alpha$ and H$n\beta$ lines with the same upper level as presented in section 6.1.5. The model predicts that under physical conditions conducive to HRL masers, the H$(n-1)\beta$ lines of high n-levels will much be brighter than the H$n\alpha$ lines due to the effects of the optical depths of the lines. If this effect is observed, it could be used as a diagnostic tool to identify regions where HRL maser might be found.

At present, there is a divide in HRL modelling between models that focus on the effects of the geometry and kinematics of the masing region, and those that prioritise the atomic physics, such as the one presented in this work. Both approaches have value, and contain important information regarding HRL masers. Ideally, these two approaches should be combined into a single model that also accounts for beaming effects. Such a model would be very complex, but will provide us with a lot of insight into HRLs. The construction of a Λ-iteration model for HRLs would be a good first step towards such a comprehensive model.

Bibliography

Aleman I., et al., 2018, MNRAS, 477, 4499

Anantharamaiah K. R., 2002, in Pramesh Rao A., Swarup G., Gopal-Krishna eds, IAU Symposium Vol. 199, The Universe at Low Radio Frequencies. p. 319

Asensio Ramos A., Elitzur M., 2018, A&A, 616, A131

Ashok N. M., Banerjee D. P. K., 2003, A&A, 409, 1007

Báez-Rubio A., Martín-Pintado J., Thum C., Planesas P., 2013, A&A, 553, A45

Báez-Rubio A., Martín-Pintado J., Rico-Villas F., Jiménez-Serra I., 2018, ApJ, 867, L6

Baker J. G., Menzel D. H., 1938, ApJ, 88, 52

Barlow M. J., 1993, in Weinberger R., Acker A., eds, IAU Symposium Vol. 155, Planetary Nebulae. p. 163

Bendo G. J., Miura R. E., Espada D., Nakanishi K., Beswick R. J., D'Cruze M. J., Dickinson C., Fuller G. A., 2017, MNRAS, 472, 1239

Bohm D., Aller L. H., 1947, ApJ, 105, 131

Bransden B. H., Joachain C. J., 2003, Physics of Atoms and Molecules. Prentice Hall

Brocklehurst M., 1970, MNRAS, 148, 417

Brocklehurst M., 1971, MNRAS, 153, 471

Brocklehurst M., Salem M., 1977a, Computer Physics Communications, 13, 39

Brocklehurst M., Salem M., 1977b, Computer Physics Communications, 13, 39

Burgess A., 1958, MNRAS, 118, 477

Burgess A., 1965, MmRAS, 69, 1

Burgess A., Summers H. P., 1969, ApJ, 157, 1007

Burgess A., Summers H. P., 1976, MNRAS, 174, 345

Chandra S., Kegel W. H., Albrecht M. A., Varshalovich D. A., 1984, A&A, 140, 295

Cox P., Martin-Pintado J., Bachiller R., Bronfman L., Cernicharo J., Nyman L.-A., Roelfsema P. R., 1995, A&A, 295, L39

Cragg D. M., Sobolev A. M., Godfrey P. D., 2002, MNRAS, 331, 521

Dickinson C., Davies R. D., Davis R. J., 2003, MNRAS, 341, 369

Douglas C. C., Lee L., Yeung M.-C., 2016, Procedia Computer Science, 80, 941

Draine B. T., 2011, Physics of the Interstellar and Intergalactic Medium. Princeton University Press

Draine B. T., Kreisch C. D., 2018, ApJ, 862, 30

Dravskikh A. F., Dravskikh Z. V., Kolbasov V. A., Misezhnikov G. S., Nikulin D. E., Shteinshleiger V. B., 1965, Dokl. Akad. Nauk SSSR, 163, 332

Dumont A.-M., Collin S., Paletou F., Coupé S., Godet O., Pelat D., 2003, A&A, 407, 13

Dupac X., et al., 2003, A&A, 404, L11

Dyson J. E., 1967, ApJ, 150, L45

Einstein A., 1916, Deutsche Physikalische Gesellschaft, 18, 318

Elitzur M., 1990, ApJ, 363, 638

Elitzur M., ed. 1992, Astronomical masers Astrophysics and Space Science Library Vol. 170. Kluwer Academic Publishers, Dordrecht

Elitzur M., 1994, ApJ, 422, 751

Elitzur M., Asensio Ramos A., 2006, MNRAS, 365, 779

Ferland G. J., et al., 2013, RMxAA, 49, 137

Ferland G. J., Henney W. J., O'Dell C. R., Peimbert M., 2016, RMxAA, 52, 261

Fujiyoshi T., Smith C. H., Caswell J. L., Moore T. J. T., Lumsden S. L., Aitken D. K., Roche P. F., 2006, MNRAS, 368, 1843

Gee C. S., Percival L. C., Lodge J. G., Richards D., 1976, MNRAS, 175, 209

Goldberg L., 1966, ApJ, 144, 1225

Gordon W., 1929, Annalen der Physik, 394, 1031

Gordon M. A., 1994, ApJ, 421, 314

Gordon M. A., Sorochenko R. L., eds, 2009, Radio Recombination Lines Astrophysics and Space Science Library Vol. 282. Springer, New York

Gordon M. A., Holder B. P., Jisonna Jr. L. J., Jorgenson R. A., Strelnitski V. S., 2001, ApJ, 559, 402

Gray M. D., Mason L., Etoka S., 2018, MNRAS, 477, 2628

Gray M. D., Baggott J., Westlake J., Etoka S., 2019, MNRAS, 486, 4216

Green L. C., Rush P. P., Chandler C. D., 1957, apjs, 3, 37

Guzmán F., Badnell N. R., Williams R. J. R., van Hoof P. A. M., Chatzikos M., Ferland G. J., 2016, MNRAS, 459, 3498

Hager W. W., 1984, SIAM Journal on Scientific and Statistical Computing, 5, 311

Hengel C., Kegel W. H., 2000, A&A, 361, 1169

Higham N. J., 1988, ACM Transactions on Mathematical Software (TOMS), 14, 381

Hoang-Binh D., 1968, Astrophys. Lett., 2, 231

Hoglund B., Mezger P. G., 1965, Science, 150, 339

Hummer D. G., Storey P. J., 1987, MNRAS, 224, 801

Hummer D. G., Storey P. J., 1992, MNRAS, 254, 277

Humphreys E. M. L., Yates J. A., Gray M. D., Field D., Bowen G. H., 2001, A&A, 379, 501

Jiménez-Serra I., Martín-Pintado J., Báez-Rubio A., Patel N., Thum C., 2011, ApJ, 732, L27

Jiménez-Serra I., Báez-Rubio A., Rivilla V. M., Martín-Pintado J., Zhang Q., Dierickx M., Patel N., 2013, ApJ, 764, L4

Kallman T., Bautista M., 2001, ApJS, 133, 221

Kardashev N. S., 1959, SvA, 3, 813

Karzas W. J., Latter R., 1961, ApJs, 6, 167

Kegel W. H., 1979, A&AS, 38, 131

Kingdon J. B., Ferland G. J., 1997, ApJ, 477, 732

Koeppen J., Kegel W. H., 1980, A&AS, 42, 59

Krolik J. H., McKee C. F., 1978, ApJS, 37, 459

Langer S. H., Watson W. D., 1984, ApJ, 284, 751

Lilley A. E., Menzel D. H., Penfield H., Zuckerman B., 1966, Nature, 209, 468

Lockett P., Elitzur M., 1992, ApJ, 399, 704

Martín-Pintado J., 2002, in Migenes V., Reid M. J., eds, IAU Symposium Vol. 206, Cosmic Masers: From Proto-Stars to Black Holes. p. 226

Martin-Pintado J., Bachiller R., Thum C., Walmsley M., 1989a, A&A, 215, L13

Martin-Pintado J., Thum C., Bachiller R., 1989b, A&A, 222, L9

Martin-Pintado J., Neri R., Thum C., Planesas P., Bachiller R., 1994, A&A, 286, 890

Menzel D. H., 1937, ApJ, 85, 330

Milne E. A., 1924, Phil. Mag., 47, 209

Murchikova E. M., Phinney E. S., Pancoast A., Blandford R. D., 2019, Nature, 570, 83

Nesterenok A. V., 2016, MNRAS, 455, 3978

Nicholls D. C., Dopita M. A., Sutherland R. S., 2012, ApJ, 752, 148

Oster L., 1961, Rev. Mod. Phys., 33, 525

Osterbrock D. E., 1962, ApJ, 135, 195

Osterbrock D. E., Ferland G. J., 2006, Astrophysics of gaseous nebulae and active galactic nuclei, 2nd edn. University Science Books, Sausalito, CA

Pengelly R. M., Seaton M. J., 1964, MNRAS, 127, 165

Petra C. G., Schenk O., Anitescu M., 2014a, IEEE Computing in Science & Engineering, 16, 32

Petra C. G., Schenk O., Lubin M., Gärtner K., 2014b, SIAM Journal on Scientific Computing, 36, C139

Planck Collaboration et al., 2014, A&A, 571, A11

Planesas P., Martin-Pintado J., Serabyn E., 1992, ApJ, 386, L23

Plaskett H. H., 1928, Harvard College Observatory Circular, 335, 1

Ponomarev V. O., 1994, Astronomy Letters, 20, 151

Ponomarev V. O., Smith H. A., Strelnitski V. S., 1994, ApJ, 424, 976

Prozesky A., Smits D. P., 2018, MNRAS, 478, 2766

Prozesky A., Smits D. P., 2020, MNRAS, 491, 2536

Reber G., Greenstein J. L., 1947, The Observatory, 67, 15

Röllig M., Kegel W. H., Mauersberger R., Doerr C., 1999, A&A, 343, 939

Rosseland S., 1926, ApJ, 63, 218

Rule E., Loeb A., Strelnitski V. S., 2013, ApJ, 775, L17

Rybicki G. B., Hummer D. G., 1991, A&A, 245, 171

Salem M., Brocklehurst M., 1979, ApJS, 39, 633

Salgado F., Morabito L. K., Oonk J. B. R., Salas P., Toribio M. C., Röttgering H. J. A., Tielens A. G. G. M., 2017, ApJ, 837, 141

Sánchez Contreras C., Báez-Rubio A., Alcolea J., Bujarrabal V., Martín-Pintado J., 2017, A&A, 603, A67

Seaton M. J., 1959, MNRAS, 119, 90

Seaton M. J., 1964, MNRAS, 127, 177

Sejnowski T. J., Hjellming R. M., 1969, ApJ, 156, 915

Smits D. P., 1991, MNRAS, 248, 193

Sobolev A. M., Cragg D. M., Godfrey P. D., 1997, A&A, 324, 211

Sorochenko R. L., Borodzich E. V., 1965, Dokl. Akad. Nauk SSSR, 163, 603

Spaans M., Norman C. A., 1997, ApJ, 488, 27

Storey P. J., Hummer D. G., 1995, MNRAS, 272, 41

Storey P. J., Sochi T., 2015a, MNRAS, 446, 1864

Storey P. J., Sochi T., 2015b, MNRAS, 446, 1864

Strelnitski V. S., Ponomarev V. O., Smith H. A., 1996a, ApJ, 470, 1118

Strelnitski V. S., Smith H. A., Ponomarev V. O., 1996b, ApJ, 470, 1134

Summers H. P., 1977, MNRAS, 178, 101

Thum C., Martin-Pintado J., Bachiller R., 1992, A&A, 256, 507

Thum C., Matthews H. E., Martin-Pintado J., Serabyn E., Planesas P., Bachiller R., 1994a, A&A, 283, 582

Thum C., Matthews H. E., Harris A. I., Tacconi L. J., Schuster K. F., Martin-Pintado J., 1994b, A&A, 288, L25

Thum C., Strelnitski V. S., Martin-Pintado J., Matthews H. E., Smith H. A., 1995, A&A, 300, 843

Thum C., Martin-Pintado J., Quirrenbach A., Matthews H. E., 1998, A&A, 333, L63

Vriens L., Smeets A. H. M., 1980, PhRvA, 22, 940

Vrinceanu D., Onofrio R., Sadeghpour H. R., 2012, ApJ, 747, 56

Walmsley C. M., 1990, A&AS, 82, 201

Weintroub J., Moran J. M., Wilner D. J., Young K., Rao R., Shinnaga H., 2008, ApJ, 677, 1140

Wiese W. L., Fuhr J. R., 2009, J. Phys. Chem. Ref. Data, 38, 565

Wild J. P., 1952, ApJ, 115, 206

Zhang Y., Zhang B., Liu X.-W., 2016, ApJ, 817, 68

Zhang Y., et al., 2019, ApJ, 886, L4

van Regemorter H., Binh Dy H., Prudhomme M., 1979, Journal of Physics B Atomic Molecular Physics, 12, 1053

van de Hulst H. C., 1945, Nederlands Tijdschrift voor Natuurkunde, 11, 230

van der Tak F. F. S., Black J. H., Schöier F. L., Jansen D. J., van Dishoeck E. F., 2007, A&A, 468, 627